Aqueous Electrochemistry of the Magnesium Surface: Thermodynamic and Kinetic Profiles

Jodie Adrian Yuwono[1,*], Nick Birbilis[1], Christopher D. Taylor[2,3], Kristen S. Williams[4], Adib J. Samin[5], Nikhil V. Medhekar[1,*]

[1] Department of Materials Science and Engineering, Monash University, Clayton VIC 3800, Australia

[2] Fontana Corrosion Center, Department of Materials Science and Engineering, The Ohio State University, Columbus OH 43210, USA

[3] Strategic Research and Innovation, DNV GL, Dublin OH 43017, USA

[4] Boeing Research and Technology, Huntsville AL 35824, USA

[5] Los Alamos National Laboratory, Los Alamos NM 87545, USA

Abstract: In this study, first-principles density functional theory (DFT) calculations are performed to investigate the contribution of each individual reaction at the magnesium/water interface. Thermodynamic and kinetic models derived from the DFT-calculated parameters are used to describe interdependent reactions at the interface and the resultant magnesium electrochemical activity at different pH and potentials. These models are able to rationalise experimental findings, such as those obtained from polarisation and immersion tests, and provide new insights for defining a complete and viable mechanism of aqueous magnesium electrochemistry.

Keywords*: magnesium, electrochemistry, corrosion, negative difference effect NDE, surface film, density functional theory DFT*

1. Introduction

Magnesium (Mg) is the lightest engineering metal with a density of ~1.7 $g.cm^{-3}$, which is significantly lower than that of aluminium (Al, ~2.7 $g.cm^{-3}$) and iron (Fe, ~7.9 $g.cm^{-3}$)[1]. Magnesium and its alloys exhibit high strength-to-weight ratios[1]. Their use enables the design of lighter engineered systems, which is beneficial for automotive and aerospace applications for reducing the energy consumption[2]. Furthermore, Mg alloys show potential to be used as viable biodegradable materials, battery electrodes and hydrogen storage materials[3–9]. Despite a great interest in Mg, there remains a persistent limitation, namely the high reactivity and high corrosion rate of Mg[10,11].

A very early investigation of Mg electrochemical activity, which here is used to described processes occurring at open circuit potential (OCP) or during polarisation, reported that Mg corrosion is accompanied with a copious release of hydrogen (H_2) gas. It was in 1866, when Beetz reported an unusual H_2 evolution (HE) in Mg during anodic polarisation[12], the first mention of so-called the negative difference effect (NDE). In 1954 Petty proposed the involvement of univalent Mg^+ ions during aqueous Mg corrosion[13]. Nonetheless, the lack of experimental evidence for Mg^+ species becomes a major barrier for this theory to advance[14–16]. Despite being a subject of numerous studies performed over the past decades, there is yet no comprehensive understanding of the mechanism of aqueous Mg corrosion and the accompanying anomalous HE. Most experimental studies have successfully identified many phenomena in aqueous corrosion of Mg alloys. For instance, the recent use of scanning vibrating electrode technique (SVET), scanning electrochemical microscopy (SECM) and atomic emission spectroelectrochemistry (AESEC) allowed the investigation of local electrochemical reactions and the detection of corresponding species at the interface[17–23]. The characterisation conveyed strong links among the formation of surface-film, anodic rate (Mg-dissolution) and cathodic rate (HE) as previously proposed[18,20,24–27]. It was revealed that the presence of impurities leads to a cathodic-activation in Mg, which is associated with the anodic HE[19,21,28–32]. However, there is at present no definitive theory that clearly describes the mechanisms of Mg interfacial reactions[33,34].

1.1. Mechanistic model of Mg electrochemical activity

The high reactivity of Mg and its alloys in aqueous environments is attributed to two main factors: i) high electronegative potential of Mg[35,36], and ii) poor protection of Mg surface-films[37,38]. Considering the Mg electrochemical activity, this metal demonstrates a very unique phenomenon known as the NDE. Normally, in most metals, e.g. platinum, copper, nickel and etc., the anodic reaction rate increases and the cathodic reaction rate decreases with increasing potential or current density[39–41]. However, Mg exhibits increasing rate of HE (which is typically known as the cathodic reaction) during anodic polarisation that apparently defies the basics of electrochemical theory. With increasing potential, the anodic reaction of Mg-dissolution is expected to increase and the cathodic reactions of water-splitting and HE are expected to decrease. Tafel-equation describes the relation approximation between electrochemical reaction rate and overpotential. The difference rationalised between theoretical predictions following Tafel-equation and experimental observations of HE in Mg describes what is so called the NDE. Moreover, Mg is a weakly polarisable metal. During anodic polarisation, Mg exhibits a high exchange current density following a small increase of anodic potential[26]. The release of high amount of hydrogen gas during anodic polarisation causes fluctuating changes of electrolyte resistance, known as ohmic drop. Consequently, this behaviour does not allow the observation of Mg electrochemical activity at a large anodic overpotential. This is also simply because of the current limit of potentiostat used nowadays that is not able to assess many decades of current following a large anodic polarisation. The NDE of Mg can be defined by the following phenomenon: the dissolution of Mg leads to increasing activity of HE (reactions 1 and 2).

$$Mg \rightarrow Mg^{2+} + + 2e^- \quad [1]$$

$$2H_2O + 2e^- \rightarrow H_2 + 2OH^- \quad [2]$$

Understanding the origins and mechanisms of anomalous HE in Mg has remained an open question for decades. In response, multiple assumptions and mechanistic models were developed[27,33,34,42–44], which lead into a debate whether the NDE remains as either a cathodic or an anodic reaction. These models are summarised and critically discussed below.

1.1.1. Partial protective surface-film and univalent Mg model

The presence of univalent Mg ion (Mg^+) was posited to be responsible for the NDE with a proposed mixed electrochemical/ chemical reactions model[14,42]. It was assumed that Mg^+ ions are produced electrochemically via a single-electron process (reaction 3), which then reacted with water and formed hydrogen gas (reaction 4). This mechanism suggested that both the rate of Mg-dissolution and the HE increased with increasing potential and current density. According to this model, the Mg^+ ions must be stable for a considerable lifetime in aqueous environments[13,45–47]. In combination with the partially protective surface-film (PPSF) model[48–50], this univalent model hypothesised that increasing film free area following an anodic polarisation will eventually lead to increasing rates of both anodic and cathodic reactions[34,42,51–54]. Anomalous HE was expected to occur at the same location of anodic Mg-dissolution[55].

$$Mg \rightarrow Mg^+ + e^- \quad [3]$$

$$Mg^+ + H_2O \rightarrow Mg^{2+} + \tfrac{1}{2}H_2 + OH^- \quad [4]$$

However, it is important to note that the Mg^+ species in aqueous environments have not been detected experimentally to date[56]. Such an accurate determination of Mg oxidation number is difficult to achieve, as it is complicated by many factors during aqueous Mg corrosion tests[57,58]. It is known that even if the Mg^+ ions exist in aqueous solution, the ions lifetime will be very short considering their spontaneous reaction with water molecules[14–16].

1.1.2. Magnesium hydride and univalent Mg model

In addition to the typical anodic and cathodic reactions, the HE was proposed to occur via a chemical reaction between magnesium hydride and water (reaction 5). The previously published Pourbaix-diagram revealed the formation of stable MgH_2 in wide range of potentials and pH values[59,60], which supports the claim that MgH_2 contributes to the NDE. MgH_2, which is expected to form following the adsorption of H^+, was believed to form at cathodic potential and decompose at anodic potential[61]. The presence of Mg^+ ions was also expected to give contribution towards the anodic HE (reaction 6). Nonetheless, the contributions of MgH_2 and Mg^+ to the NDE have never been validated experimentally.

$$MgH_2 + 2H_2O \rightarrow Mg^{2+} + 2OH^- + 2H_2 \quad [5]$$

$$Mg^+ + H^+ \rightarrow Mg^{2+} + \tfrac{1}{2}H_2 \quad [6]$$

Recently, a new theory considering the role of MgH_2 as a metastable species, which helps the production of hydrogen gas during anodic polarisation was proposed[62]. It was hypothesised that MgH_2 is formed beneath the nature oxide film and exhibits a more significant role to support the formation of H_2 than that of surface films and noble impurities. However, the role of hydride remains unclear.

1.1.3. Enhanced surface-film catalytic activity and impurities enrichment model

According to this model, the dissolution of magnesium at the OCP and anodic potential was proposed to occur via a double-electron dissolution reaction (reaction 1) in which the NDE is driven by two factors, i.e. surface-film and impurities. First, the study by Williams and co-workers.[17] revealed that the Mg surfaces become more active in supporting the HE with the formation of surface-film. This mechanism, called the cathodic-activation, suggested that the film formed upon the surface has an ability to catalyse the HE following: i) the transformation of prior anodic areas into later cathodic areas, and ii) the expansion of cathodic areas with time[17–19,63–65]. Second, increasing HE rate over time was caused by the enrichment of impurities on the Mg surface following dissolution. Many studies revealed that the noble impurities were accumulated in the surface-film with a higher concentration than that in the bulk metal[21,31,32,66–68]. Following their dissolution from Mg matrix, there is a possibility of noble impurities re-deposit on the surface, and acting as remote cathodic active sites[31,69,70]. It was understood that the NDE occurs as the result of a persistent development of cathodic reaction, which was dictated by the formation and growth of dark film areas and the enrichment of noble impurities on the surface. Considering this mechanism, the primary source of HE was believed to occur at or near the dark film areas[18,71,72]. However, to date, there are conflicting reports about the role of surface-film in supporting the anodic HE in Mg[20,27,64,65,71,73,74]. The recent studies by Fajardo[28,75,76] indicated that the HE contributions from the surface-film and noble impurities were insignificant compared to the overall rate of anodic HE. This was confirmed by the study of Lysne[68], which suggested that the efficiency of impurities to the anodic HE is insignificant; revealing that impurities are not primarily responsible for the overall NDE.

1.1.4. Enhanced surface catalytic activity model

A recent model used to explain the NDE considered the catalytic nature of dissolving Mg surface[27,28,75–77]. Magnesium, as a highly reactive metal in aqueous environments, spontaneously oxidises and also catalyses other interfacial reactions (e.g. HE). It was observed that the surface catalytic activity changes with the changes of surface-dissolution rate, as observed in experiments reporting that the exchange current density for the HE increased with increasing Mg-dissolution rate[77]. The primary source of HE was believed to occur in the anodic region where Mg-dissolution occurs. The availability of active sites for interfacial reaction is essential in this theory. The activation occurs following the breakdown of MgO and $Mg(OH)_2$ films and the dissolution of surface in the presence of chloride ions (Cl^-), while the deactivation occurs following the saturation and adsorption of OH^- on the surface. According to this model, increasing surface catalytic activity is a major contributor for the anodic HE observed in Mg[28,75,76,78]. However, a complete understanding of Mg surface catalytic activity remains unknown and more evidence is required to support this theory to advance.

As summarised above, experimental approaches cannot provide a complete understanding of complex mechanisms of reactions at surfaces and interfaces, mainly because most experimental insights are derived from the rate measurement, which consists of several elementary steps that occur simultaneously[42,45,58,79]. The present analytical tools found their limit for capturing the real-time molecular processes during aqueous Mg corrosion[80,81]. Complementary to the experimental approaches, quantum chemical simulations can be used as a valuable tool[82–86] to provide additional insights into aqueous Mg electrochemical activity[35,36,87–91]. For the past recent years, first-principles calculations are increasingly being used for

describing thermodynamic profiles of Mg under different conditions such as for developing Pourbaix diagrams[36,92,93]. The investigations of kinetic profiles of Mg using first-principles calculations also offers new possibilities to explore various electrochemical reactions and validate different theories proposed for Mg electrochemistry[35,88,90,94]. Different additional factors such as alloying elements, anions and grain-boundaries have been introduced separately in the models of first-principles calculations[87,91–95]. Despite the capabilities to obtain accurate prediction of Mg electrochemistry, these methods are limited in the size and complexity of simulation model. Until now, first-principles DFT calculations cannot effectively simulate a system under electric field (such as during polarisation) and a system with large number of atoms that consists of multiple species (alloying elements and ions). This reveals that the scope of first-principles DFT investigations are limited in a very small system and the findings have to be used in combination with other results obtained from different methods, including the experiments.

Herein, this approach is used to develop a model for Mg/H_2O electrochemical system, revealing its unique information at the molecular level during interfacial reactions. This study aims to provide a fundamental and comprehensive understanding of aqueous Mg electrochemical activity using first-principles density-functional-theory (DFT) methods, as detailed in Computational Methods (section 2). The Results and Discussion (section 3) is organised as follows. Section 3.1 investigates the thermodynamic stability of various Mg species in water, considering the formation of complex species with different oxidation-states. Section 3.2 develops the kinetic profile of aqueous Mg electrochemical activity, which includes various reactions at the Mg/H_2O interface, capturing the complexities of aqueous Mg corrosion such as that observed during a real-time process. Section 3.3 studies the formation of surface-film ($MgO/Mg(OH)_2$) and its thermodynamic stability on the Mg(0001) surface, following the interaction with water molecules. Section 3.4 explores the formation of electrochemical double layer (EDL) of water molecules on the Mg(0001) surface. The results from the DFT-calculations are then rationalised with the experimental observations in section 3.5, in which a complete mechanism of Mg electrochemical activity in aqueous environments was developed and validated accordingly.

2. Computational Methods

Herein, two first-principles DFT-calculations methods are employed: i) molecular-orbital and ii) plane-wave DFT methods. The molecular-orbital DFT is highly efficient for studying electronic structure of isolated molecules, and is used for screening different possible structures of Mg species in water. On the other hand, the plane-wave DFT is highly efficient for studying the electronic structures of solids and surfaces, and consequently is utilised for developing the electrochemical profiles of Mg/H_2O system. The molecular-orbital DFT-calculations for Mg atom with explicit water (H_2O), hydroxide (OH), hydrogen (H) and oxygen (O) in both neutral and positive charged-states were implemented using Spartan "14 v1.1.4 molecular modelling software[96]. The geometries of Mg species were constructed—using Spartan graphical model builder—, optimised and calculated using RB3LYP/6.311G* basis set with SM5.4/A water solvation model[97,98]. For each calculation, atomic charges of Mg and its species were calculated using the Weinhold's natural population analysis (NPA) method[99]. The computed electronic energies were then used to calculate the reaction and ionisation enthalpies for different species.

The plane-wave DFT-calculations were implemented using Vienna ab initio software package[100,101] (VASP) with energy cut-off of 500 eV. The approximations for electron exchange and correlation were carried out using the generalised gradient approximation (GGA) and the revised Perdew-Burke-Ernzerhof (RPBE) functional[102–104]. In all cases, a Γ centred k-points grid for sampling the Brillouin zone was employed. Geometrical optimisations were achieved by relaxing all ionic positions as well as supercell vectors until the Hellman-Feynman forces were less than 0.01 eV $Å^{-1}$. The interactions between surface and environment were modelled using “slab method”, with a semi-infinite surface was calculated using six layers of Mg periodically extended in the x and y directions and separated by 30 Å vacuum layer in the z-direction. The bottom two layers were fixed while the upper four layers were relaxed to obtain a surface-bulk like configuration. In contrast to previous studies, which often simplified their model by using an implicit water solvent[36,89,91], this study provides a better understanding of the interfacial reactions and EDL structure by using explicit water molecules were introduced on the Mg(0001) surface[105]. The nudged elastic band (NEB) method[106,107] was used to investigate different pathways of Mg interfacial reactions considered in this study.

3. Results and Discussion

3.1. Thermodynamic stability of Mg species in water

To probe all possible Mg species in water[108], different structures of $Mg\text{-}xH_2O$, Mg-xOH, Mg-xH and Mg-O (defined as Mg complex species) are considered for geometry optimisation. The structures were optimised in neutral and positive charged-states (+1 and +2). The reaction and ionisation enthalpies for each Mg species were calculated using Spartan (Table S1). Magnesium atom readily bonds with water molecules, and forming either $Mg\text{-}xH_2O$ or Mg-xOH and x/2 H_2. The ionisation energy of Mg species decreases with increasing number of bonds with water molecules, as shown in Figure 1. The lowest energy-configuration is found in $Mg\text{-}6H_2O$. From the geometry optimisation, it is revealed that some Mg species, such as in

Mg-2H_2O and Mg-3H_2O complexes, are not stable in +2 charged-state. However, as Mg atom bonds with more water molecules, such as in Mg-5H_2O and Mg-6H_2O complexes, the formation of +2 charged-state becomes more favourable. It is important to note that the charged-state of Mg species is not similar to the Mg atom oxidation-state (Table S2). The natural population analysis (NPA) method is used to calculate the charge on Mg atom. Magnesium atom shares electron with the neighbouring atoms (H and O); thus, it is unlikely for Mg to have nominally full atomic charge of +2.

The requisite energies for Mg ionisation are ranked from the lowest to the highest as follows: i) from Mg to Mg^+, ii) from Mg^+ to Mg^{2+} and iii) from Mg^{2+} to Mg^{3+}. Divalent magnesium ion, Mg^{2+} is found as the most stable oxidation-state for Mg atom. This is because further ionisation to Mg^{3+} requires electron removal from an inner shell, which demands an extensive amount of energy that cannot be supported or compensated by any natural processes. The first stage of Mg ionisation (from Mg to Mg^+) is stable in vacuum, but not available in aqueous environments. The ionisation energy from Mg to Mg^+ and from Mg^+ to Mg^{2+} is 7.7 and 68.6 eV, respectively. Meanwhile, the ionisation energy from Mg-6H_2O to $[Mg\text{-}6H_2O]^+$ and from $[Mg\text{-}6H_2O]^+$ to $[Mg\text{-}6H_2O]^{2+}$ is 3.1 and 15.0 eV, respectively. The requisite ionisation energy decreases when Mg bonds with H_2O, H^+ and OH^-. Despite the ionisation energy for Mg^{2+} being higher than that of Mg^+, the bonding of Mg with water molecules facilitates the formation of Mg^{2+} species from Mg and Mg^+ species at lower enthalpies. This denotes that the ionisation of Mg in the complex form occurs more favourably than in its atomic form. For instance, the ionisation energy for two most stable Mg species in aqueous environments, viz. Mg-6H_2O and Mg-4H_2O-2OH are presented in Table 1. It is revealed that the total ionisation-reaction enthalpy could be achieved at a slightly lower enthalpy in a simultaneous process compared to that in consecutive individual processes. The results imply that Mg^{2+} readily forms complex species of $[Mg\text{-}6H_2O]^{2+}$ in aqueous environments. Therefore, it is expected that during aqueous Mg corrosion, the "dissolving" Mg atom from the surface will directly transform into a divalent ion of Mg complex species.

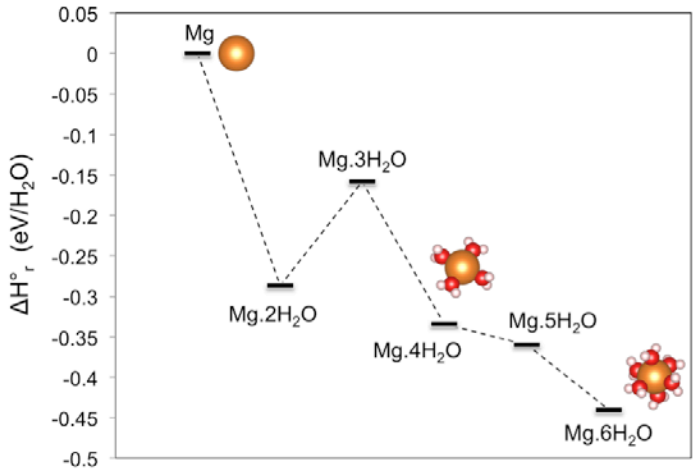

Figure 1. Reaction enthalpy of Mg atom with water molecules forming Mg.$(H_2O)_x$ complexes in aqueous environments

Table 1. The DFT-calculated reaction enthalpy for Mg complex in aqueous environments

Structure	Reaction enthalpy - ΔH°_r (eV per functional unit)				
	0 → +1	0 → +2	+1 → +1	+1 → +2	+2 → +2
Mg-6H_2O	0.473	15.502	-7.255	7.775	-60.867
Mg-4H_2O-2OH	1.401	13.690	-6.326	5.963	-62.679

Note:

$\Delta H^\circ_{r_{Mg-6H_2O\,(0\rightarrow+1)}} = H^\circ_{Mg-6H_2O^+} - H^\circ_{Mg} - 6\,H^\circ_{H_2O}$

$\Delta H^\circ_{r_{Mg-6H_2O\,(+1\rightarrow+1)}} = H^\circ_{Mg-6H_2O^+} - H^\circ_{Mg^+} - 6\,H^\circ_{H_2O}$

$\Delta H^\circ_{r_{Mg-6H_2O\,(+1\rightarrow+2)}} = H^\circ_{Mg-6H_2O^{2+}} - H^\circ_{Mg^+} - 6\,H^\circ_{H_2O}$

3.2. Kinetic profiles of Mg interfacial reactions in water

3.2.1. Construction of the kinetic model

Magnesium interfacial reactions proposed in this study are listed below with the following assumptions in order to understand Mg electrochemical behaviour in water. The construction of the Mg kinetic model was based on the parameters obtained from the first-principles calculations, theoretical literatures and standard reference databases. The Arrhenius-equation (equation 7) with the existing prefactor[109,110] (A) and calculated energy barrier (E_a) was used to estimate the rate constants, $k_1 – k_7$ (Table S3).

$k_0 = A \exp(-E_a / RT)$ [7]

According to the conservation law, the total number of surface sites is conserved based on the system-constraint (Equation 8). This constraint denotes a fixed number of available sites for adsorption on the Mg(0001) surface, up to a single monolayer (1 ML). In this case, the presence of subsurface *O is considered as the surface adsorption, *O, similar to the adsorption of *H and *OH. The reaction kinetic equations (equations 9 – 15) exhibit the rate of surface site changes considering the production and consumption of Mg*, Mg*OH, Mg*H and Mg*O. To simulate the effect of different pH and background Mg^{2+} concentrations, the Nernst-equation was introduced into Arrhenius-equation. Several combinations of $[Mg^{2+}] = 2 \times 10^{-5}$ M and pH = 1, 3, 5, 7, 9, 11, 13 were used in the construction of Mg surface kinetic profiles[90]. Equations 16 – 19 were then solved under steady-state conditions i.e. with the time-derivatives set to zero to obtain the steady-state coverage and reactions rate profile.

Constraint of the system

$\theta_M + \theta_H + \theta_{OH} + \theta_O = 1$ [8]

Reaction kinetic equation

Water-splitting: $2Mg^* + H_2O \rightarrow Mg^*OH + Mg^*H$ [9]

$K_1 = k_1\theta_M^2$

Tafel-HE pathway: $2Mg^*H \rightarrow 2Mg^* + H_2$ [10]

$K_2 = k_2\theta_H^2$

*OH-desorption: $Mg^*OH + e^- \rightarrow Mg^* + OH^-$ [11]

$K_3 = k_3\theta_{OH}$

Mg-dissolution via OH: $Mg + Mg^*OH \rightarrow Mg^* + Mg^{2+} + OH^- + e^-$ [12]

$K_4 = k_4\theta_{OH}$

Heyrovsky-HE pathway: $Mg^*H + H^+ + e^- \rightarrow Mg^* + H_2$ [13]

$K_5 = k_5\theta_H$

*OH-dissociation: $Mg^*OH + Mg \rightarrow Mg^*O + Mg^*H$ [14]

$K_6 = k_6\theta_{OH}$

Mg-dissolution via O: $Mg + Mg^*O + H_2 \rightarrow Mg^* + Mg^{2+} + H_2O + 2e^-$ [15]

$K_7 = k_7\theta_O$

Reaction kinetic model

$d\theta_M/dt = -2k_1\,\theta_M^2 + 2k_2\,\theta_H^2 + (k_3 + k_4)\,\theta_{OH} + k_5\,\theta_H + k_7\,\theta_O$ [16]

$d\theta_H/dt = k_1\,\theta_M^2 - 2k_2\,\theta_H^2 - k_5\,\theta_H + k_6\,\theta_{OH}$ [17]

$$d\theta_{OH}/dt = k_1 \theta_M^2 - (k_3 + k_4 + k_6)\, \theta_{OH} \quad [18]$$

$$d\theta_O/dt = k_6 \theta_{OH} - k_7 \theta_O \quad [19]$$

3.2.2. Investigation of Mg interfacial reactions in water from first-principles

3.2.2.1. Water-splitting reaction

The splitting of water molecules on Mg(0001) surface with the co-adsorption of OH^- and H^+ is investigated by incorporating a water bilayer network. This process is equivalent to the consumption of two available metal sites (Mg*) on the surface (reaction 9). The previous study by Williams and co-workers considered this process up to a water dimer configuration[88]. In the presence of network of water molecules, the energy barrier for water-splitting reaction increases due to the hydrogen-bonding in water molecules. The water-splitting energy barriers with monomer and dimer configuration are 0.87 and 1.06 eV[88], respectively. It is thus necessary to consider the water-splitting mechanism on the surface from a more complex network, since it can provide an accurate prediction closer to the real-interactions between Mg surface and water layer[105,111–115].

A water bilayer configuration with six water molecules is introduced above the Mg surface. Different configurations for water molecules, for example, with hydrogen atoms of H_2O molecules pointing away from the surface (H-up), towards the surface (H-down) or with H_2O molecules parallel to the surface (flat) are considered (Figure S1). The water-splitting energy barriers vary based on the orientation of hydrogen relative to the surface, which is affected by potential, pH and the presence of adsorbed species. From the NEB calculation, H-down water molecule has the least energy barrier of 2.73 eV to dissociate into H^+ and OH^-, while H-up and flat water molecules have the energy barriers of 3.87 and 3.74 eV, respectively. It is observed that in the single bilayer water-network, the interaction between water molecules is -0.26 eV per H_2O molecule, while after the dissociation of a single water molecule, the interaction between water molecules decreases to -0.23 eV per H_2O molecule. It means that the water-splitting reaction reduces the interaction between the water molecules. For instance, in the dimer structure, the binding between water molecules is less stronger (with -0.09 eV per H_2O molecule) than in a larger water network. The changes of the energy barrier as a function of the structure of water molecules can be interpreted as a catalytic mechanism for Mg interfacial reactions, where the weakening of the hydrogen bond networks in water contributes to decreasing energy barrier for the following water-splitting reaction. This mechanism can be explained as follows. The active Mg surface attracts a water molecule from an ordered structure of water bilayer network. The water molecule near the surface dissociates and adsorbs as *H and *OH. Following the disruption of water bilayer network (due to the preceding water-splitting), the succeeding water-splitting reaction occurs with a lower energy barrier; thus progressing at a higher rate than that of the preceding reaction.

The water-splitting reaction is posited to occur in water molecules with a weak hydrogen bond network, such as in monomer and dimer configurations. Considering that the low rate of water-splitting reaction from bilayer network is expected the rates of other interfacial reactions may be influenced. The result therefore contradicts the fact that the water-splitting reaction is expected to occur spontaneously[35,36]. This inconsistency reveals that the properties of water layer near the surface are different from the properties of water layer far from the surface, the bulk water[112,113,116]. The changes of surface conditions (e.g. the impurities enrichment, the surface oxidation and the surface hydroxylation) may alter the interaction between Mg surface and water layer; thus, creating a unique water layer configuration at the interface, which behaves differently from the bulk water.

3.2.2.2. Hydrogen-evolution reaction

Following the splitting of water molecules and the adsorption of hydrogen, hydrogen atoms on the surface can recombine (and form H_2) via either Tafel or Heyrovsky mechanism[117–120]. These two mechanisms are considered herein for the construction of Mg kinetic model. The Tafel pathway is a homolytic reaction type with no electron transfer process (chemical reaction). It means that the variation of the potential has no significance for the changes of reaction rate. This mechanism becomes more significant with the occurrence of *OH-desorption, as described in the previous study[90]. Meanwhile, the Heyrovsky pathway is a heterolytic reaction type with an electron transfer process (electrochemical reaction). Consequently, the Heyrovsky reaction rate is sensitive to the changes of potential and pH.

In the Tafel reaction, two *H from Mg*H sites recombine and produce H_2, leaving two available Mg* sites (reaction 10). This reaction along with the *OH-desorption is deemed to be responsible for the cathodic HE. In the *OH-desorption reaction, one *OH from Mg*OH site desorbs from the surface, leaving one available Mg* site (reaction 11). The Tafel reaction rate depends on the hydrogen coverage (θ_H). In the Heyrovsky reaction, one *H from Mg*H site recombines with H^+ from the solution, producing H_2 and leaving one available Mg* site (reaction 13). Adsorbed hydrogen (*H) is a negatively charged species due to the interaction with Mg surface. The Heyrovsky reaction rate varies according to the changes of potential, pH and θ_H. Using NEB calculations, the energy barriers for the Heyrovsky and Tafel mechanisms are obtained as 1.08 and 1.31, respectively (Figure S2 and S3, respectively). It is shown that the Heyrovsky reaction is the dominant pathway for HE on the Mg surface, as it occurs with a lower energy barrier than that of the Tafel reaction. To support this claim obtained from the static 0 K DFT-calculations, molecular dynamics (MD) calculations at 298 K were also performed, in which the results

exhibit consistent findings: the Heyrovsky mechanism is more favourable than the Tafel mechanism. The hydrogen-recombination occurs with the energy barrier and reaction enthalpy of 0.7 and -0.3 eV, respectively (Figure S4).

3.2.2.3. Mg-dissolution reaction

There are two dissolution mechanisms that are proposed in this study: i.) a water-assisted and ii.) a hydroxide-assisted dissolutions. The dissolution of Mg from the surface is investigated using the model previously developed[121]. Herein, the dissolution process is simulated with an adsorbed Mg atom on the Mg(0001) surface in vacuum and in the presence of explicit water molecules. The adsorbed Mg atom, which is bonded with H_2O or OH^-, is sequentially displaced to 5.5 Å above the surface. Initially, an oxygen-assisted dissolution mechanism is considered. However, during the geometrical optimisation, it is found that oxygen reacted with the water molecules and converted into two *OH groups, which then facilitated the Mg-dissolution from the surface (as if it follows the hydroxide-assisted mechanism). The water-assisted Mg-dissolution, a double-electrons transfer mechanism, has an energy barrier of 2.51 eV with the dissolving Mg atomic Bader charge[122,123] of +0.72 and +1.82 at the initial and final states, respectively (Figure S6). Meanwhile, the hydroxide-assisted Mg-dissolution, a single-electron transfer mechanism, has an energy barrier of 4.32 eV with the dissolving Mg atomic Bader charge of +0.93 and +1.46 at the initial and final states, respectively (Figure S6). These findings validate the results obtained in section 3.1 regarding the formation of divalent ions of complex Mg species. The Bader charge calculations also give a confidence that there is a formation of positive charged Mg complex species in both mechanisms.

In addition to these mechanisms as derived from the NEB calculations, which exhibit high-energy barrier for Mg-dissolution, the cohesive energy for Mg ionic solids is considered. This attempt has also been applied in earlier study by Taylor[90]. The cohesive energies for Mg, MgO and $Mg(OH)_2$ are -1.50, -10.22 and -21.52 eV, respectively and these are consistent to the previous studies[87,124,125]. This indicates that the energies requisite to break ionic-bonding in bulk MgO- and $Mg(OH)_2$-systems are higher than to break metallic-bonding in bulk Mg-system.

From the NEB and cohesive energy calculations, it is revealed that the dissolution of Mg occurs primarily via the water-assisted mechanism in the clean Mg surface. The dissolution of Mg from the surface covered by the film requires more energy than in the clean surface, indicating that the film-covered surface may act as a local cathode. A selective surface-dissolution may occur in the regions where there are no films or surface contaminants. For the construction of Mg reaction kinetic model, the energy barrier for reactions 7 and 10 is set to be identical to 1.50 eV. This is based on the assumption that the effect of Mg*O to the surface-dissolution was negligible, knowing that the oxygen will adsorb on the surface and diffuse into the bulk.

3.2.2.4. Hydroxide-dissociation reaction

The films formed on the Mg surface have diffuse bilayer structures, made of MgO as the inner film and $Mg(OH)_2$ as the outer film[34,126]. The previous DFT-calculations revealed that the film stability is sensitive to the presence of surface impurities, e.g. alloying elements (from the metal) and anions (from the environment)[89]. However, there remains a gap in the understanding for the formation of bilayer films as observed in many experiments[66,126–131]. Herein, the absorption of O from *OH on the surface to the bulk Mg was considered, where the formation of a bilayer film can be understood with the presence of *O in the Mg subsurface (as the inner MgO layer) and *OH on the Mg surface (as the outer $Mg(OH)_2$ layer). During the hydroxide-dissociation reaction, oxygen moves to the available subsurface site and hydrogen remains on the available surface site. The adsorbed hydrogen (*H) then recombines with another adsorbed *H or H^+ ion and evolves as H_2 gas. There are two mechanism of *OH-dissociation investigated for the differences in the Tafel- and Heyrovsky-HE (Figure S6). Considering these reaction pathways, the energy barrier for *OH-dissociation is calculated to be 1.08 eV. It is found that the presence of *H (and other surface contaminants) on the surface affects the *OH-dissociation process as observed from the energy differences between the two plots. Further investigation about the formation of surface-film composed of Mg*O and Mg*OH on the Mg(0001) surface is discussed in section 3.3. It is important to note that the kinetic model built herein does not consider the changes of surface morphology during the chemisorption of elemental O into Mg lattice.

3.2.3. Implementation of the kinetic model

In this study, the Mg surface electrochemical activity as the functions of potential and pH is successfully developed using the kinetic model based on the DFT-calculated parameters. Individual contribution of elementary reactions is shown in Figure 2. It is worth noting that this contribution is valid when all the reactions proposed in section 3.2.1 are fully considered when solving the steady-state equation. The surface coverage plots at different pH values, considering the competitive production and consumption sites of Mg*, Mg*OH, Mg*H and Mg*O (Figure S7), denotes that the rates of interfacial reactions are sensitive to the dynamics of surface coverage. It is known from this study that the concentration of Mg*OH on the surface increases with increasing pH and is found at the overpotential regions near the OCP. The range of overpotential for Mg*OH concentration becomes wider in alkaline conditions than that in acidic conditions. Cathodic potential regions are dominated by Mg*, while anodic potential regions are dominated by Mg*H. Compared to a previous finding[90], there is no significant Mg*H concentration available on the surface during cathodic polarisation, as this model considers a new mechanism for HE, known as the Heyrovsky reaction. This pathway facilitates a more rapid desorption rate of hydrogen than the Tafel reaction. In addition, the concentration of Mg*O is negligible in any conditions, indicating that Mg*O is more dominant to be formed in

the substrate than on the surface. This implies a rapid diffusion rate of oxygen into bulk or alternatively a slow dissociation rate of hydroxide from the surface. On the other hand, the presence of MgO as inner film in the experiments is expected to form before the immersion in aqueous electrolytes or during the contact between Mg and atmosphere. In principle, the surface coverage, which varies according to the potential and pH, plays an important role for controlling the reactions at the Mg/H_2O interface. This denotes that the thermodynamic stability of Mg surface dictates the competition among the water-splitting, hydroxide-desorption and hydroxide-dissociation, hydrogen-evolution and Mg-dissolution reactions on the surface. Overall, the effect of pH to the interfacial reactions can be summarised as follows, with decreasing pH (from alkaline to acidic conditions):

- The rates of water-splitting, hydroxide-desorption and Heyrovsky-HE reactions increase,
- The rate of Tafel-HE reaction decreases,
- The rates of hydroxide-dissociation and Mg-dissolution reactions increase at anodic regions and decrease at cathodic regions, respectively,
- The OCP shifts to a nobler value.

The rates of water-splitting reaction change with the changes of pH and potential. Overall, the water-splitting reaction occurs at higher rates in acidic conditions than that in alkaline conditions. Increasing anodic potential leads to the fluctuating rates of water-splitting near the OCP, which then continues to decrease with a larger anodic overpotential. This alteration is mainly caused by the increasing coverage of Mg*OH and Mg*H on the surface, where water-splitting reaction prefers take place on the clean surface to the covered surface (noting the effect of surface-passivation). Two different HE pathways considered in this study exhibit that the HE does not follow the normal Tafel cathodic slope, where the HE rate is expected to decrease with increasing potential. The Tafel chemical hydrogen-recombination pathway becomes more favourable with increasing hydrogen coverage on the surface following the increase of anodic potential. Meanwhile, the Heyrovsky rates fluctuate at the narrow overpotential regions near the OCP (showing the NDE) before they continue to decrease with increasing anodic potential. This denotes that the Heyrovsky electrochemical hydrogen-recombination pathway dictates the production of H_2 during cathodic polarisation, which invalidates the formation of stable Mg*H species[59,132], and both the Heyrovsky and Tafel pathways dictate the production of H_2 during anodic polarisation. Hydroxide-dissociation and hydroxide-desorption reactions play an important role for controlling the rates of other reactions, since they control the availability of active sites on the surface, where the water-splitting, Mg-dissolution and HE reactions occur only on the clean surface and not on the hydroxide-covered surface.

From this kinetic model, the rates for hydroxide-desorption are higher than those for hydroxide-dissociation. However, the hydroxide-desorption rates decrease significantly with increasing anodic potential and pH. It is important to note that during anodic polarisation, the hydroxide-desorption reaction is accompanied by the dissolution of Mg atoms from the surface, where the Mg-dissolution reaction rate increases with increasing anodic overpotential. There are two types of hydroxide-desorption mechanisms: i) direct pathway during cathodic polarisation and ii) indirect pathway during anodic polarisation. Slow hydroxide-dissociation reaction rate denotes that the diffusion of oxygen into bulk may also negligible, as the hydroxide-desorption is found to be more dominant process. These mechanisms, hydroxide-desorption and hydroxide-dissociation, are critical for maintaining the availability of active sites[59,90] as they convert Mg*OH into Mg*.

The HE rates presented herein are the combination of both the Tafel (reaction 10) and Heyrovsky (reaction 13) reactions, while the Mg-dissolution rates are the combination of both single- (reaction 12) and double-electron (reaction 15) dissolution reactions. The DFT-calculated polarisation curves for Mg(0001) surface in water (Figure 3) give credible predictions of Mg electrochemical activity that are in agreement with the experimental polarisation curves for pure Mg. The cathodic polarisation curves resemble the process of water-splitting reaction that is equivalent to the HE, while the anodic polarisation curves resemble the process of Mg-dissolution reaction.

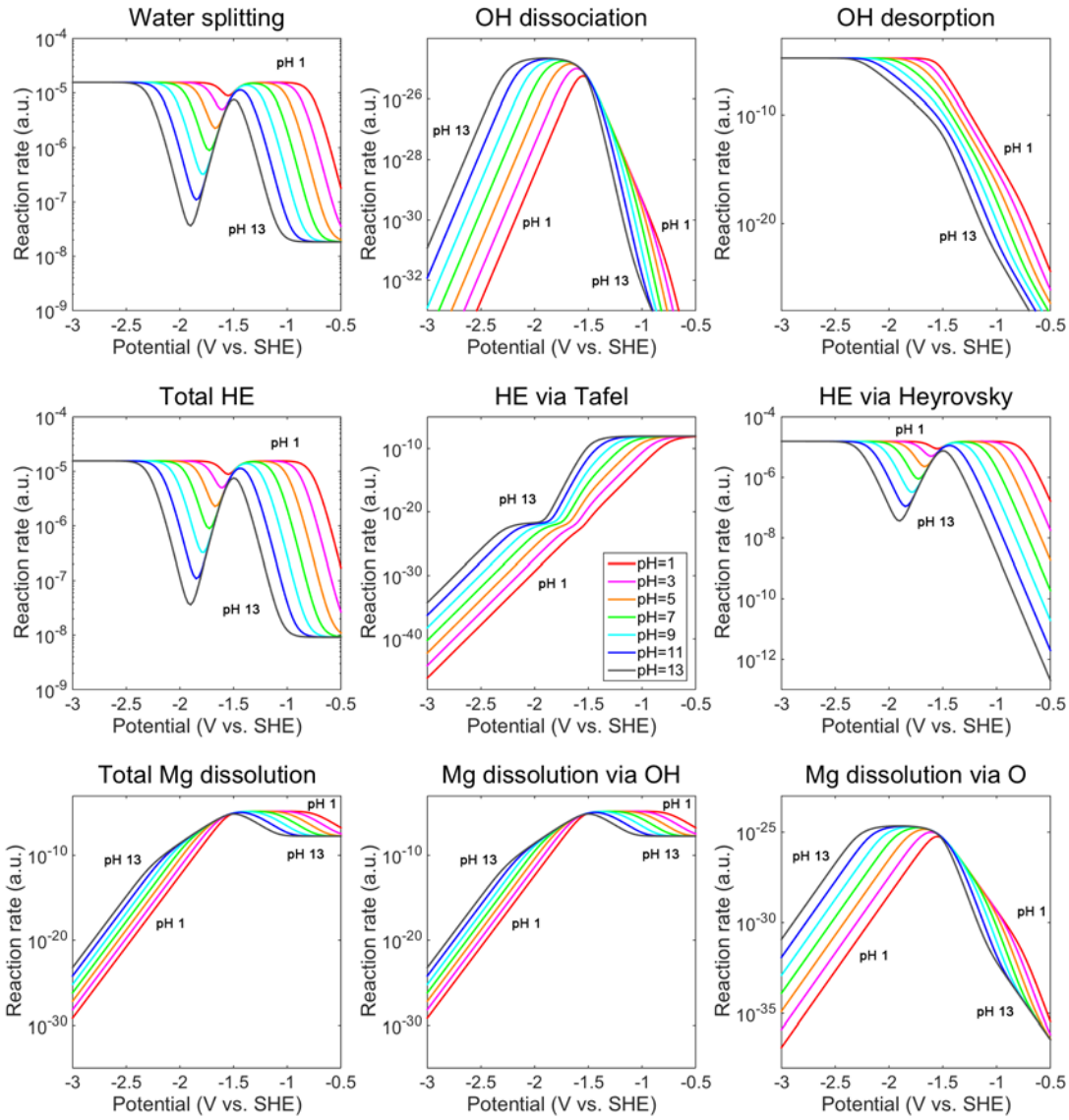

Figure 2. Kinetic profiles of various elementary reactions on the Mg(0001) surface as the functions of potential and pH

In addition, the NDE of Mg is observed at any pH, and the difference between cathodic and anodic HE increases with increasing pH. This means that the NDE becomes more dominant with the formation of bilayer films of $MgO/Mg(OH)_2$, which is in agreement with the previous findings[20,65,133,134]. Increasing pH makes the NDE manifested over wider cathodic and anodic overpotential ranges. The rates of HE are the lowest at the OCP, and increase with increasing cathodic and anodic overpotentials. However, the rates of HE then tend to decrease at larger anodic overpotential. The trends found herein seem to be inconsistent with the previous theory about the catalysing surface-film[20,73,89]. Firstly, the formation of bilayer films, especially Mg*OH is supposed to enhance the rates of water-splitting and HE, which means that HE rate in alkaline conditions should be higher than that in acidic conditions[20]. Secondly, the rates of anodic HE keeps on increasing even at a large anodic overpotential[64,71,134–136]. The reasonable explanations for the difference, which also becomes the limitation of the present kinetic model, can be listed as follows:

- This model does not consider the formation of different features on the surface due to the preceding interfacial reactions that may develop micro-galvanic cells,
- This model does not consider the changes of active sites due to the preceding interfacial reactions that may alter the succeeding interfacial reactions[28,65,66,137–141],
- This model does not consider the evolution of the surface morphology, especially due to Mg-dissolution that may enrich the concentration of noble impurities on the surface[21,28,29,31,66,142].

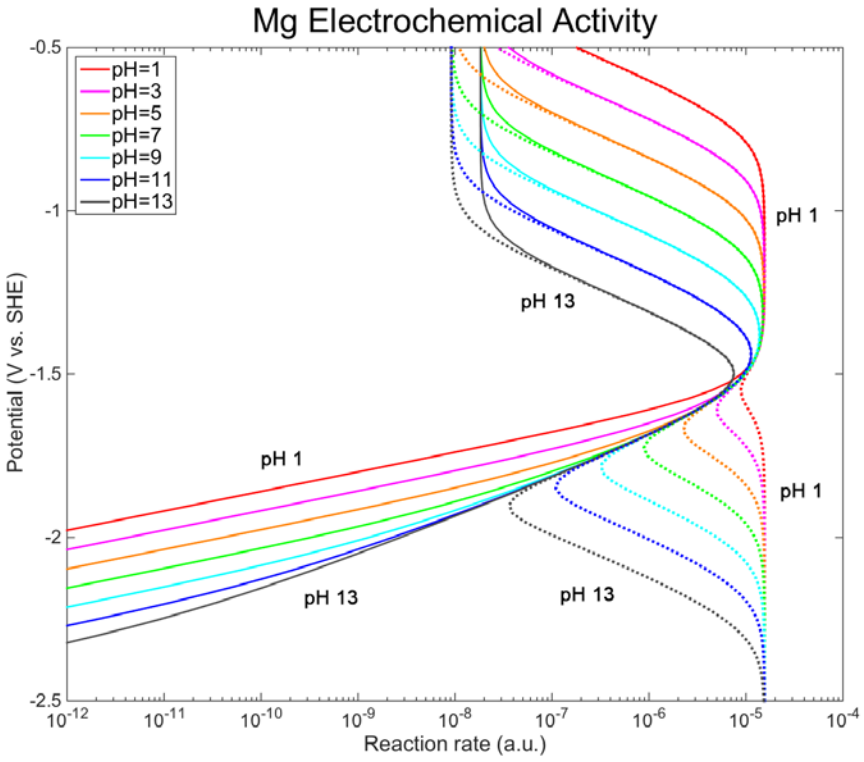

Figure 3. The DFT-calculated polarisation curves for Mg electrochemical activity in aqueous environments at different pH values, showing cathodic (water-splitting/ HE – dotted lines) and anodic (Mg-dissolution – solid lines) branches

Consistent with the results presented in section 3.2.1, both reactions 12 and 15 can be assumed to occur via a double-electron dissolution process. However, in reaction 12, a single hydroxide ion reacts with Mg^{2+} as if the dissolution occurs with the formation of an $Mg(OH)^{+}$ ion complex. Different mechanisms of Mg-dissolution are captured well using these two reactions, in which reaction 12 is sensitive to the potential and pH and reaction 15 is sensitive only to the potential. The energy barrier for Mg-dissolution reactions is approximated using the cohesive energy of bulk Mg solid, as the previous calculations using NEB cannot produce sensible values for both reactions. The rates of Mg-dissolution increase with increasing anodic overpotential, in which the rates at cathodic regions are higher in alkaline conditions than that in acidic conditions, while the rates at anodic regions are higher in acidic conditions. It is believed that at cathodic regions, the positive contribution of electrode potential for reducing activation energy is compensated by the negative contribution of pH. However, it is worth noting that Mg-dissolution is mainly recognised as the anodic reaction, in which the trends obtained in this model are in agreement with the experiments[143]. Considering that corrosion rate of Mg is the balance between anodic and cathodic reactions, the corrosion rate of Mg is higher in acidic conditions than that in alkaline conditions. In accordance with enhanced surface catalytic activity theory, the kinetic model also exhibits slightly higher Mg-dissolution rates than that of HE. This denotes that the formation of actively dissolving Mg surface may correspond to the occurrence of anodic HE. This once again emphasises the importance of active sites for the occurrence of interfacial reactions, in which it is driven by the dissolution of Mg at anodic regions.

3.3. Formation of oxide and hydroxide film on the Mg surface

The mechanistic basis for the formation of bilayer film ($MgO/Mg(OH)_2$ formation following the partial (reaction 20) and complete water-splitting reactions (reaction 21), is sought to be understood next. The films formed upon the Mg surface in aqueous environments are diffused bilayer structures made of a thick-porous $Mg(OH)_2$-rich outer-layer and a thin-dense MgO-rich inner-layer[34,126]. Experiments have shown that the concentration of $Mg(OH)_2$ decreases and MgO increases with an increasing depth of the film from the surface[131,144]. However, the kinetic model developed in the previous section indicates a negligible oxygen surface coverage (Mg*O). This is mainly because the current model does not consider the presence of oxygen in the substrate (subsurface – where it is typically found in the experiments), also noting that the dissociation of hydroxide occurs at lower rates than the desorption of hydroxide from the surface. It is important to understand the interaction between the covered surface (Mg surface with adsorbed species: Mg*O and Mg*OH) with water molecules, as it may represent the realistic experimental conditions. The partial and complete splitting of a water molecule can be represented as:

$H_2O \rightarrow *OH + *H$ [20]

$H_2O \rightarrow *O + 2\,*H$ [21]

The reaction enthalpies for partial and complete water-splitting are calculated from the formation energies of $Mg*O_x$, $Mg*(OH)_y$ and $Mg*O_x(OH)_y$, as shown in Figure 4. The DFT-calculated energies for Mg*O and Mg*OH formations are presented in Table 2. It is observed that the complete water-splitting reaction on the surface, which is accompanied with higher amount of H_2 gas release per H_2O molecule, has a more negative reaction enthalpy than that of the partial water-splitting reaction. With the formation of Mg*O on the surface, water-splitting still occurs favourably on the surface, although with decreasing enthalpy per H_2O molecule. This means that the formation of $MgO/Mg(OH)_2$ film (modelled as MgO*OH) can be achieved spontaneously on the Mg(0001) surface altogether with H_2 gas production through the series of complete and partial water-splitting reactions. In addition, the strong thermodynamic driving force obtained from Mg/MgO transformation to Mg/MgO/MgOH suggests that the surface is continually oxidised in aqueous environments by simultaneously forming mixed oxide and hydroxide films.

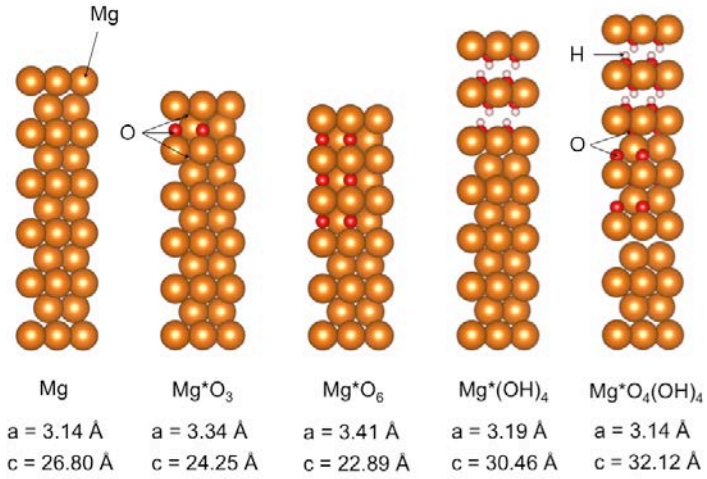

Figure 4. Optimised geometries of (2x2x1) Mg supercell used for the transformation study of Mg surface forming an oxidation film of MgO, $Mg(OH)_2$ and $MgO/Mg(OH)_2$

Table 2. The DFT-calculated reaction enthalpy for the Mg surfaces transformation during the interaction with water molecules in aqueous environments

Electrochemical Reaction	ΔH_r (eV per H_2O)
$Mg + 3H_2O \rightarrow Mg*O_3 + 3H_2$	-2.76
$Mg + 6H_2O \rightarrow Mg*O_6 + 6H_2$	-2.67
$Mg + 4H_2O \rightarrow Mg*(OH)_4 + 2H_2$	-1.67
$Mg + 8H_2O \rightarrow Mg*O_4(OH)_4 + 6H_2$	-1.90
$Mg*O_3 + 5H_2O \rightarrow Mg*O_4(OH)_4 + 3H_2$	-2.32
$Mg*O_3 + H_2O + H_2 \rightarrow Mg*(OH)_4$	1.58
$Mg*O_3 + 3H_2O \rightarrow Mg*O_6 + 3H_2$	-2.59
$Mg*O_6 + 2H_2O \rightarrow Mg*O_4(OH)_4$	3.93

During the transformations from Mg to Mg*O and Mg*OH, the volume changes of crystal structure are expected, where Mg*O and Mg*OH cause the contraction and expansion of the structure, respectively. The lattice parameters of the corresponding supercell containing those structures are presented in Figure 4. The change is obvious in the lattice parameter of z-axis, whose value is altered by -9.5% and 13.6% from that of the Mg supercell with the formation of Mg*O and Mg*OH, respectively. This is consistent with the experimental findings which suggest the formation of thin-dense MgO and thick-porous $Mg(OH)_2$ films from the occurrence of both partial and complete water-splitting reactions[34,66,126–130]. As water molecule dissociates and oxygen adsorbs on the surface, crystalline MgO nucleates and grows laterally forming an oxide-cluster, followed by the precipitation and thickening process[145,146]. At later stages, because of the continuous hydration on the surface,

crystalline MgO experiences severe breakdown (volume expansion) forming $Mg(OH)_2$ via the dissolution-precipitation reactions[131].

Herein, the formation and growth of the bilayer film is studied using hexagonal close-packed (hcp) crystal structures of Mg, MgO and $Mg(OH)_2$ with (0001) surface orientation. The results obtained here provide qualitative information that is beneficial for predicting the electrochemical activity trends for different compounds. This is particularly important to understand the evolution of surface activity following the occurrence of preceding interfacial reactions, e.g. water reduction. The effects of potential and local pH on the thermodynamic stability and catalytic role of film can be examined from the DFT-calculated Pourbaix-diagrams developed for different surfaces: Mg(0001), MgO(0001) and $Mg(OH)_2$(0001). Firstly, the Mg(0001) surface interaction with H_2O as expressed by the complete and partial water-splitting reactions is presented in Figure 5a. All competing electrochemical reactions (reactions 22 – 28) that occur on the Mg(0001) surface are outlined in Table S4 with their corresponding DFT-calculated Nernst-equations.

$$Mg + x\ H_2O \leftrightarrows Mg^*(OH)_x + x/2\ H_2 \quad [22]$$

$$Mg + x\ H_2O \leftrightarrows Mg^*O_x + x\ H_2 \quad [23]$$

$$Mg^*(OH)_x \leftrightarrows Mg^*O_x + x/2\ H_2 \quad [24]$$

$$Mg_{1v} + [Mg(H_2O)_6]^{2+} \leftrightarrows Mg^*(OH)_x + 2[(H_3O)(H_2O)]^+ + (1\text{-}x/2)\ O_2 + (1\text{-}x/2)\ H_2 \quad [25]$$

$$Mg_{1v} + [Mg(H_2O)_6]^{2+} \leftrightarrows Mg^*O_x + 2[(H_3O)(H_2O)]^+ + (1\text{-}x/2)\ O_2 + H_2 \quad [26]$$

$$Mg + 2[(H_3O)(H_2O)]^+ + 2H_2O \leftrightarrows Mg_{1v} + [Mg(H_2O)_6]^{2+} + H_2 \quad [27]$$

$$Mg + x/2\ H_2 \leftrightarrows Mg^*H_x \quad [28]$$

The clean Mg(0001) surface, hydroxylated Mg(0001) surface, oxidised Mg(0001) surface and Mg(0001) surface with one surface vacancy are represented by Mg, $Mg^*(OH)_x$, Mg^*O_x and Mg_{1v}, respectively. Meanwhile, the hexa-hydrated Mg ion and hydronium ion are represented by $[Mg(H_2O)_6]^{2+}$ and $[(H_3O)(H_2O)]^+$, respectively.

As shown in Figure 5a, increasing *O coverage shifts the phase boundary between Mg and Mg*O to the right while increasing *OH coverage shifts the phase boundary between Mg and Mg*OH to the left. The transformation from MgO to $Mg(OH)_2$ occurs at a large anodic overpotential from the OCP which denotes that this process requires significant amount of energy. In addition, it is found that the reaction enthalpy for surface hydroxylation above 1 ML becomes more endothermic with increasing surface coverage (Figure S8). The presence of excess *OH groups leads to a structural disorder (rearrangement) of surface atoms, which can potentially explain the formation of porous $Mg(OH)_2$ film. A unit cell of the hcp Mg contains two Mg atoms while a unit cell of hcp $Mg(OH)_2$ contains one Mg atom. This suggests that the formation of two hcp $Mg(OH)_2$ unit cell (1x1x2) is equivalent to the breakdown of one hcp Mg unit cell (1x1x1). The DFT-calculated Pourbaix-diagram for the Mg(0001) surface indicates that during anodic polarisation, water molecules first dissociate according to reaction 21, which then dissociate according to reaction 20 with increasing potential. During this process, both Mg*O and Mg*OH are formed on the surface and their presence alters the overall electrochemical behaviour on the Mg(0001) surface, especially when the adsorbates diffuse into the bulk Mg and form stable MgO and $Mg(OH)_2$ crystals that have different electrochemical properties. It is posited therefore that the water-splitting reaction initiates the formation of micro-galvanic cells at different regions on the surface.

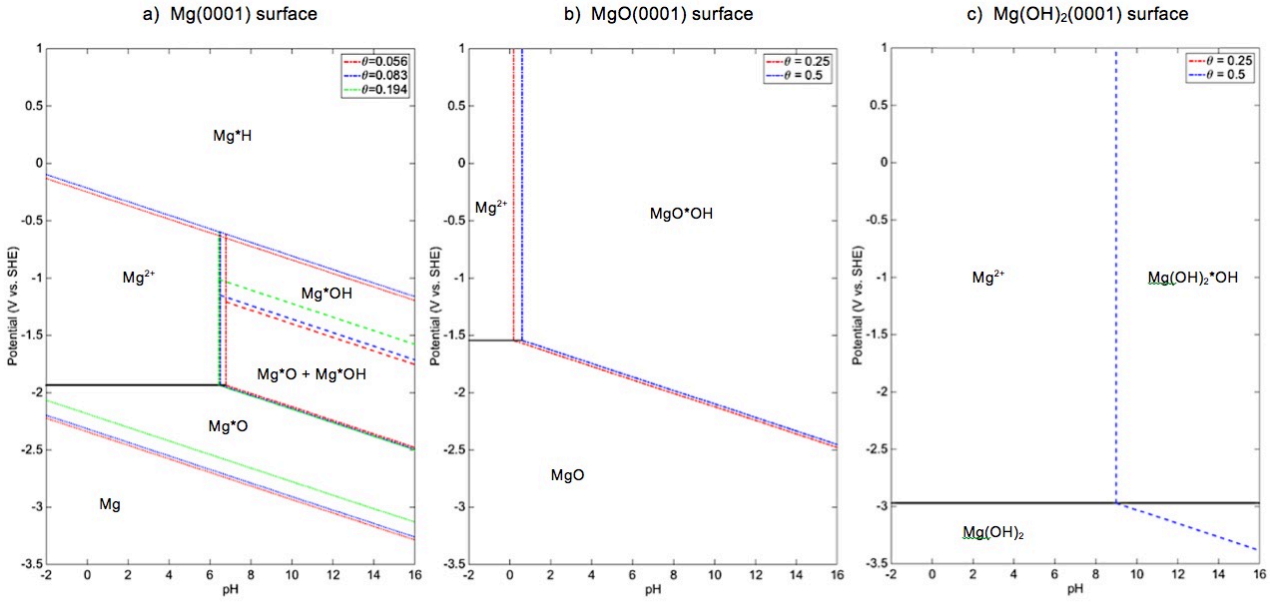

Figure 5. The DFT-calculated Pourbaix-diagrams of (0001) surfaces of hcp Mg (a), MgO (b) and $Mg(OH)_2$ (c) in aqueous environments

Secondly, as the previous calculation in section 3.2 only considers the presence of surface *O on the Mg(0001) surface, this calculation considers the presence of subsurface *O in the bulk Mg as the MgO(0001) surface. The competing electrochemical reactions (reactions 29 – 31) and their corresponding DFT-calculated Nernst-equations are presented in Table S5. The preliminary study reveals that the *OH favourable adsorption sites on the MgO(0001) surface are fcc hollow, hcp hollow and a-top with the adsorption energies of -1.91, -1.34 and -1.0 eV per H_2O, respectively. The dissolution potential of MgO, -1.543 V vs. SHE, is nobler than that of Mg, -1.934 V vs. SHE (Figure 5b). This reveals that MgO acts as the cathode and Mg acts as the anode during the electrochemical processes in aqueous environments.

$$MgO + x\ H_2O \leftrightarrows MgO^*(OH)_x + x/2\ H_2 \quad [29]$$

$$MgO_{1v} + [Mg(H_2O)_6]^{2+} \leftrightarrows MgO^*(OH)_x + 2[(H_3O)(H_2O)]^+ + (1\text{-}x/2)\ O_2 + (1\text{-}x/2)\ H_2 \quad [30]$$

$$MgO + 2[(H_3O)(H_2O)]^+ + 2H_2O \leftrightarrows MgO_{1v} + [Mg(H_2O)_6]^{2+} + H_2 \quad [31]$$

Thirdly, the electrochemical interactions between $Mg(OH)_2$(0001) surface and water molecules were studied as the functions of potential and pH. It is revealed that hollow sites remain as the most favourable adsorption sites for *OH with the adsorption energy of -1.21 eV per H_2O which is much weaker than the previous two surfaces. The corresponding DFT-calculated Nernst-equations of three competing electrochemical reactions (reactions 32 – 34) are listed in Table S6. The $Mg(OH)_2$(0001) surface Pourbaix-diagram is presented in Figure 5c. It is understood that the surface readily dissolves into Mg^{2+} with increasing potential at any pH. There is no favourability of the surface to form additional hydroxide-film. This is because every Mg atom is already bonded with two *OH groups. Therefore, the behaviour of $Mg(OH)_2$ in promoting surface-dissolution will ensure continuous consumption of Mg atoms from the surface, which is equivalent to a thickening mechanism of $Mg(OH)_2$ film.

$$Mg(OH)_2 + x\ H_2O \leftrightarrows Mg(OH)_2{}^*(OH)_x + x/2\ H_2 \quad [32]$$

$$Mg(OH)_{2\ 1v} + [Mg(H_2O)_6]^{2+} \leftrightarrows Mg(OH)_2{}^*(OH)_x + 2[(H_3O)(H_2O)]^+ + (1\text{-}x/2)\ O_2 + (1\text{-}x/2)\ H_2 \quad [33]$$

$$Mg(OH)_2 + 2[(H_3O)(H_2O)]^+ + 2H_2O \leftrightarrows Mg(OH)_{2\ 1v} + [Mg(H_2O)_6]^{2+} + H_2 \quad [34]$$

Following the oxidation of Mg surface, the formation of insulating film made of MgO and $Mg(OH)_2$ is expected to affect the occurrence of charge transfer reactions, both thermodynamically and kinetically. In this study, MgO and $Mg(OH)_2$ (0001) surfaces are not completely oxidised, where outer Mg layer still have active sites that can facilitate charge transfer reactions. This is evidenced from negative reaction enthalpies of hydroxide adsorption and Mg dissolution reactions (Tables 2, S5 and S6). Although, these reactions are thermodynamically favourable, the formation of insulating film can significantly decrease the reactions kinetic. Such behaviour is observed in previous section, showing that increasing *OH coverage decreases the rates of water splitting and HE reactions (Figures 2 and S7). Further investigations considering different possible Mg electrochemical reactions on oxidised Mg surface are required to clarify the role of surface film and its electronic conductivity on the electrochemical reactions at Mg/H_2O interface.

3.4. Configuration of electrochemical double layer at the Mg/H_2O interface

Water structures were optimised by considering the water-water and metal-water interactions, using the RPBE D-3 functional to yield a correct wetting behaviour on the Mg(0001) surface[147–156]. There are many different water structures that are very close in energy (Figure S9). The trend for water-cluster formation is determined based on the competition between hydrogen-bonding and metal-water bonding (Table S7), in which the formation of proton donor and acceptor is significant for controlling the thermodynamic and kinetic properties of water EDL. This behaviour can be used to explain the intrinsic characteristics of water molecules on the metal surface, whose structures often undergo cluster-formation and bulk-evolution[111,116].

The single water molecule adsorbs through its oxygen atom at a-top site with the adsorption energy of -0.41 eV per H_2O. A more refined structure with 2.22 Å Mg-O interatomic distance is obtained by considering van der Waals effect. The adsorption energy increases with increasing number of water molecules adsorbed on the surface (Table S7). Dimer water molecules exhibit different interactions on the surface, indicating the competition between hydrogen-bonding among water molecules and metal-water bonding at the interface. The upper water molecule, which is weakly bonded to the metal surface, acts as a proton acceptor, while the water molecule nearest to the surface, which is strongly bonded to the metal surface, acts as a proton donor[112]. This buckled water structure is normally found in the dimer configuration, where the upper water molecule favours stronger hydrogen-bonding between water molecules than water molecules near the surface. This behaviour manifests in the shift from the ideal a-top adsorption sites by 0.20 and 0.49 Å with 2.78 Å O-O interatomic separation between water molecules. In addition, there were two different configurations in trimer and tetramer water molecules considered, i.e. cyclic and open structures. The ground-state structure for water trimer is found in the open structure with the

adsorption energy of -0.51 eV per H_2O, which consists of two proton donors and one proton acceptor. The ground-state structure for water tetramer is found in the cyclic structure with the adsorption energy of -0.54 eV per H_2O molecule.

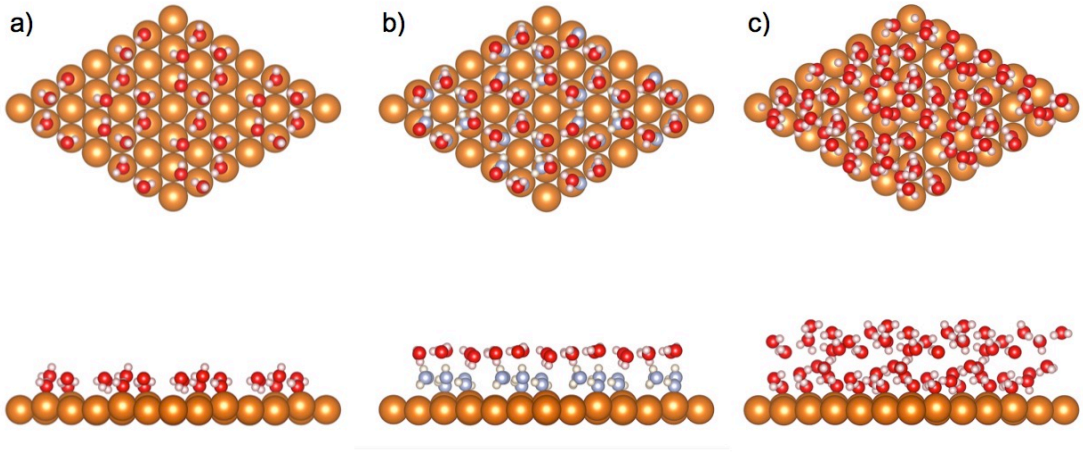

Figure 6. Top and side view of the optimised geometries for the water EDL on the Mg(0001) surface with (a) single, (b) double and (c) triple water bilayer structure

Moreover, the single bilayer (water hexamer), double bilayer and triple bilayer water structures were built to better understand the bulk configuration of water molecules on the Mg(0001) surface (Figure 6). The model of bulk water structure with six water molecules is in agreement with experiments, in which the structure has a density of 5 x 10^{14} cm^2 at a water dose of 1 x 10^{-6} mbar[157]. In the single bilayer water structure, the interaction between water molecules increases with all six water molecules interconnecting together and forming an ice Ih(0001) water bilayer structure[158]. In the double bilayer and triple bilayer water structures, a three-dimensional network of tetragonal and hexagonal structure is formed, respectively. This finding is consistent with increasing binding energy observed among water molecules. As a result, the cluster formation of water molecules reduces the interaction between Mg surface and water molecules, as their molecular interactions are increasingly being more dominant with the incorporation of more networks of water molecules. In this study of water bilayer configurations, there is a significant increase of binding energy between water molecules from -0.26 eV per H_2O molecule for single bilayer to -0.43 eV per H_2O molecule for triple bilayer along with a slight change of the water adsorption energy on the surface from -0.53 eV per H_2O molecule for single bilayer to -0.55 eV per H_2O molecule for triple bilayer.

Herein, the energy barrier for water-splitting reaction is found to be sensitive to the hydrogen-bonding within the water molecules as well as the surface conditions. For instance the dissociation of water molecules from the dimer and single bilayer structure requires the energy of 1.06[88] and 2.73 eV, respectively. The energy barrier for water-splitting reaction is thought to increase with increasing number of water molecules present on the surface. By considering high reactivity of Mg in aqueous environments, this water-splitting reaction can be expected to initiate in the region where hydrogen-bonding within water molecules is weak (or in the region where metal-water bonding is dominant), e.g. regions with noble impurities. The occurrence of continuous water-splitting reaction accelerates the subsequent water-splitting, mainly because the preceding reaction disrupts the configuration of water bilayer network that weaken the hydrogen-bonding between water molecules. Meanwhile, from the kinetic model developed in the previous section, the water-splitting energy barrier on the MgO or $Mg(OH)_2$ surface is not taken into account; therefore, the rate of water-splitting decreases with the formation of Mg*OH on the surface. Nonetheless, it is found that the single bilayer water structure is altered on the hydroxylated Mg(0001) surface with θ_{OH}=1, showing stronger hydrogen-bonding of -0.28 eV per H_2O molecule than that on the clean Mg(0001) surface. From the surface Pourbaix-diagrams, the dissociation of water molecules on the MgO(0001) surface becomes more favourable across the wide range of pH compared to that on the Mg(0001) surface. This clarifies the experimental findings which suggest that H_2 emerges at or near the surface-film region[18,38,66,159].

3.5. Discussion of Mg electrochemical activity in water

Experimental literatures, as presented in section 1.1, reported several models to explain the source and mechanism of high HE rates on the anodically polarised Mg. This distinctive phenomenon, the so-called NDE, is only found in the Mg and active metals[160].

Previously, it was proposed that Mg^+ ions exist in the solution, they will be readily attacked by water molecules and have a very short lifetime[14–16]. However, this behaviour is clarified in section 3.1 — it is found that Mg readily reacts with H_2O, OH^- and H^+ and instantaneously forming a stable +2 charged Mg species. The magnesium hydride (MgH_2) intermediate model is

also no longer relevant, as the present study highlights a more favourable mechanism for hydrogen-recombination via the Heyrovsky reaction at the cathodic potentials. In the previous kinetic model[90], the Tafel reaction is the only mechanism considered for hydrogen-recombination, in which the formation of hydrogen-rich surface (Mg*H) is possible due to a lower hydrogen-recombination rate. As presented in section 3.2, the Heyrovsky reaction occurs at a higher rate, therefore the surface has equivalent rates for both the hydrogen-adsorption and hydrogen-desorption processes. This finding is supported by the DFT-calculated Pourbaix-diagram developed for the Mg(0001) surface in water as elaborated in section 3.3. Moreover, a recent study also confirmed a favourable Heyrovsky pathway on Mg surface, which is expected to occur only during polarisation and not at the OCP[161]. The polarisation was expected to facilitate lateral transfer of surface charge following the changes of adsorption behaviour. In this study, it is evident that Mg*OH prefers to form within the potential ranges near at the OCP (depends on pH), and decreasing the Heyrovsky reaction rate.

The HE reaction in Mg cathodic and anodic potentials is described from a water-splitting reaction, which consists of three steps: i) Volmer (reaction 9), ii) Tafel (reaction 10) and iii) Heyrovsky (reaction 13). The cathodic (β_c) and anodic (β_a) Tafel slopes for HE is presented in Figure 7 and Table S8. It is known that from the literature the values of β_c and β_a were $\geq$ 200 mV/decade and $\leq$ 150 mV/decade, respectively. In combination with the experiments, the values of β_c and β_a obtained from the simulations at different pH values are presented in Table 3. The Tafel slopes of Mg are sensitive towards the changes of pH at the interface and the values of β_c and β_a are within the normal ranges as suggested from the experiments. However, the DFT-calculated polarisation curve herein denotes the inversion of anodic curves for Mg-dissolution at a large anodic overpotential, which has never been reported previously in the experiments. This behaviour is difficult to obtain in real-tests mainly due to the difficulties in normalising the effect of voltage drop from the electrolyte resistance that varies according to electrolyte conditions. It is commonly known that most of the anodic Tafel slopes from the experiments are over-corrected since the electrolyte resistance is often approximated with a single fixed value[77,143]. It is important to note that the results obtained from DFT calculations of Mg(0001) surface in water have certain limitations during modelling, meaning that the findings could not be directly compared with the experimental results. However, such modelling does permit for focusing future experiments required to better understand Mg electrochemistry in aqueous electrolytes. In this case, this study does not consider factors such as natural oxide film, crystal orientation (surface plane), grain size, alloying element, intermetallic particle and ion, which will definitely give a significant change of Mg electrochemical properties.

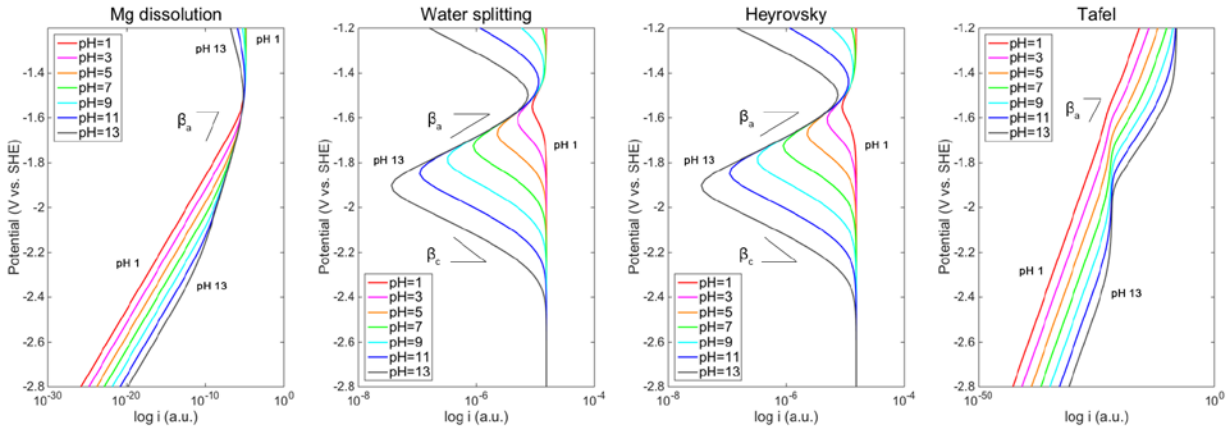

Figure 7. Cathodic and anodic branches determined from reactions 4, 5 and 8 with their corresponding Tafel slopes (β) are listed in Table S8

The previous studies proposed the formation of magnesium hydride (MgH_2) at cathodic and anodic potentials[60,61,132]. However, from the kinetic model presented in section 3.2, the formation of Mg*H is only observed at a large anodic overpotential. Although there is a high *H coverage on the surface, the rate of hydrogen-recombination via Tafel pathway is lower than that of via Heyrovsky pathway. The claim that the Tafel anodic HE contributes to the NDE at a large anodic overpotential is confirmed. However, the major contributor of anodic HE in this condition may also come from the noble impurities enrichment on the surface. A high rate of Mg-dissolution reaction at this potential range increases the noble impurities concentration on the surface, which in turn creates micro-galvanic cells between different surface features, including the film. In addition, the claim of MgH_2 forms at cathodic region is not observed[59,162], in both the kinetic and thermodynamic models presented in section 3.2 and 3.3, respectively. In contrast, the results denote a favourable formation of MgO at the potential range near the OCP, whose value changes with pH.

Aqueous Mg electrochemical activity can be understood from the latest popular model which combines the contributions of surface-film, noble impurities and surface catalytic activity to the anodic HE. In the surface-film based model, the H_2 gas emerges at or near the region of a dark film on the surface. This dark film is characterised as the bilayer structure composed of MgO and $Mg(OH)_2$. The study by Casey[38] proposed that the overall Mg corrosion is determined by the rate of ions transported through the surface-film. It is now known that the formation of this film does not effectively protect the underlying metal surface, which is mainly due to two factors: i) the Pilling-Bedworth ratio of Mg surface-film is smaller than 1, and ii) the $Mg(OH)_2$ film dissolves in the acidic conditions. Although it is known to be ineffective, the formation of film greatly influences Mg interfacial reactions in aqueous environments. A poor protection of the surface-film triggers the formation of micro-galvanic cells on the surface, where Mg, MgO and $Mg(OH)_2$ have different electrochemical behaviours in aqueous environments (section 3.3). This results into the simultaneous increase of the HE and Mg-dissolution rate at a small anodic overpotential. This mechanism is consistent with a recent model[143], which suggested the enhancement of surface catalytic activity. A preservation of active sites is found to be essential for maintaining continuous interfacial reactions, and herein it is achieved via *OH desorption and Mg dissolution reactions. Following the increase of Mg-dissolution rate on the surface, the HE rate also increases. The accumulation of noble impurities on the surface can provide an additional contribution to the anodic aqueous activity of Mg. The NDE increases with increasing rates of breakdown of the film and dissolution of Mg. The breakdown of the film reveals that MgO surface favours the water-splitting reaction and consequently the HE. Meanwhile, the dissolution of Mg surface atoms will cause the dislodgement of noble impurities, which in turn redeposit on the surface and take an active part in the electrochemical reactions as the cathode. This mechanism is particularly important for the NDE of Mg since the enrichment of noble impurities might be important for increasing aqueous Mg activity at a large anodic overpotential, in which the anodic HE in clean Mg surface obtained herein indicates decreasing trends. Otherwise, the behaviour of Mg observed at a large anodic overpotential here may represent the real behaviour of Mg that is not captured during the experiments. It is difficult to large anodically polarised Mg, considering that Mg is weakly polarisable metal and the current limit of present potentiostat.

Table 3. Comparison of Tafel slope calculated in this study and reported in the literature

Material	Tafel Determination Method	OCP (V vs. SHE)	β_a (mV dec^{-1})	β_c (mV dec^{-1})	pH	Electrolyte	Ref.
Pure Mg	Simulation Tafel extrapolation	-1.50	127.65	346.42	3	H_2O	This study
Pure Mg	Simulation Tafel extrapolation	-1.65	146.13	170.82	7	H_2O	This study
Pure Mg	Simulation Tafel extrapolation	-1.80	141.61	135.72	11	H_2O	This study
CP Mg	Experimental Tafel extrapolation	-1.38	31.0	186.0	-	NaCl	[163]
CP Mg	Experimental Tafel extrapolation	-1.31	150.0	315.0	5.4	NaCl	[26]
CP Mg	Experimental Tafel extrapolation	-1.29	58.0	246.0	-	NaCl	[163]
CP Mg	Experimental Levenberg-Marquardt	-1.35	54.5	334.5	-	NaCl	[164]
CP Mg	Experimental Levenberg-Marquardt	-1.35	50.0	304.7	-	NaCl	[164]
CP Mg	Experimental Levenberg-Marquardt	-1.31	82.0	260.0	-	NaCl	[165]
CP Mg	Experimental Levenberg-Marquardt	-1.06	31.5	183.0	-	NaCl	[165]
CP Mg	Experimental Tafel extrapolation	-1.31	27.0	168.0	-	NaCl	[166]

The formation of MgO is considered as two-step processes of partial water-splitting followed by *OH-dissociation, rather than one-step process of complete water-splitting. Furthermore, the dynamic surface changes that occur due to the interfacial reactions are not fully considered in the construction of kinetic model. The interfacial reactions were only studied as the functions of potential, pH and surface adsorbates. Therefore, the changes of energy barrier as the formation of surface defects, which arrives from the surface-dissolution and water-splitting reaction, are not established herein. The mechanisms and energy barriers for interfacial reactions may be slightly different in the defective surface than that in the perfect surface, because of the changes of interaction with other species, i.e. H_2O, H^+ and OH^-. Due to this factor, the estimation of rate constants from each pH does not allow an accurate prediction of the Mg reactions absolute rate. The model constraint used herein assumes that each site of the metal is occupied before another layer of adsorbates can form. A moving boundary condition will permit the quantification of reaction rate and thus offers an accurate prediction of reaction rate as the functions of potential, pH and Mg^{2+} concentration. Moreover, this study did not take into account the transport of ions towards and away from the surface. This is especially important to understand the catalytic activity of surface-film at different conditions. In this study, the (0001) surfaces are chosen considering that they are the highest close-packed surface, where corrosion tends to attack; while also building a better understanding of the early oxidation process when Mg develops Mg*O and Mg*OH. The trends obtained using theoretical studies of the kinetic behaviour of pure Mg are in remarkable agreement with the experimental studies of the aqueous Mg electrochemical activity. Therefore, the approximations made on the Mg(0001) surface are expected to represent the overall electrochemical behavior of pure Mg in aqueous environments.

The most frequent and reliable mitigation strategy used for improving Mg electrochemical resistance is achieved by either changing the composition (via alloying) and the microstructure or modifying the surface properties (via coating)[43,167–171]. However, since the mitigation strategies remain ineffective due to a lack of fundamental understanding of aqueous Mg corrosion mechanism, this study offers a new approach for understanding the aqueous electrochemical activity of pure Mg. It is known that the Mg surface electrochemical reactions consist of different complex reactions, in which their rates are controlled by different parameters (i.e. overpotential, pH, corrosion products, impurities and anions). Reflecting that many Mg-based applications do not only interact with water molecules, it is important to also consider the contribution of surface defects and crystal orientation, alloying elements in the Mg and anions in the solutions. Those factors are not fully considered herein since this study primarily focuses on providing a mechanistic basis for the aqueous electrochemical activity of pure Mg. However, the studies considering several of those aspects have been previously investigated by Yuwono and co-workers[92].

4. Conclusions

Persistent challenges in the understanding of aqueous Mg electrochemistry have been clarified using first-principles DFT calculations; including addressing: i) the oxidation-state of Mg, ii) the nature of surface-film, and iii) the role of alloying elements (impurities). The holistic overview of the electrochemical response of Mg in aqueous environments is presented, where the contribution of each individual reaction is elaborated. It is revealed that the aqueous Mg electrochemistry consists of a series of chemical and electrochemical reactions that are associated with the presence of adsorbed species (*OH, *H and *O). Periodic DFT calculations are used to map the minimum energy pathways (MEP) for different Mg interfacial reactions in water as well as to understand the formation of bilayer films and water EDL structures on the surface.

The electrochemical response (including corrosion and during polarisation) of Mg in water is also determined based on the changes of potential and pH. Herein, the contribution of the Tafel-HE pathway is determined to be small, and increases at a large anodic overpotential. Meanwhile, the contribution of the Heyrovsky-HE pathway is large at both cathodic and anodic overpotentials. It is observed that to support continuous HE, both the *OH-desorption and Mg-dissolution reactions play prominent role in providing active sites for the water-splitting reaction. In acidic conditions, the rates of *OH-desorption (at cathodic potential) and Mg-dissolution (at anodic potential) reach their maximum along with the rates of water-splitting and the Heyrovsky-HE (at both cathodic and anodic potentials). The so-called NDE is smaller without the formation of stable Mg*OH, which influences other interfacial reactions, particularly water-splitting and HE. In neutral and alkaline conditions, the surface accommodates the formation of stable Mg*OH, causing the HE occurs at a significantly lower rate at OCP than that at both cathodic and anodic overpotentials. The simulations performed in the present study reveals Tafel slopes similar to the experiments at both cathodic and anodic polarisations.

The formation of bilayer films is investigated by characterising the electrochemical behaviour of Mg, MgO and $Mg(OH)_2$ (0001) surfaces in aqueous environments. Electrochemical activities are plotted as the functions of potential and pH. It is revealed that the formation of surface-film made of thin-dense MgO as the inner-layer and thick-porous $Mg(OH)_2$ as the outer-layer occurs spontaneously in aqueous environments. Both MgO and $Mg(OH)_2$ surfaces exhibit different electrochemical responses towards the water-splitting, *OH adsorption and HE compared to those exhibited by a clean Mg surface. In addition, since the oxidation film does not completely cover the surface, the formation of micro-galvanic cells on the surface could lead to increasing electrochemical activity.

The water EDL structure on the Mg(0001) surface denotes the correlation between the energy barrier for water-splitting reaction and the complexity of the network of water molecules near the surface. A successive water-splitting reaction on the surface is desired as it accelerates the reaction rate by weakening the water-water interaction or strengthening the metal-water interaction. The presence of adsorbed species, e.g. *OH and *H on the surface also alters the interaction between Mg surface and water molecules in a bilayer network.

Furthermore, the catalytic activity of surface-film during the Mg interfacial reactions is sought to be clarified, and it could be explained by the formation of Mg*O/ Mg*OH and the disruption of water layer network at the Mg/H_2O interface. These two factors are considered as the major contributors for the NDE of Mg, where anodic HE is observed together with Mg-dissolution. Meanwhile, the enrichment of noble impurities and the enhancement of surface catalytic activity are deemed to be important for supporting the anodic HE only at a large anodic overpotential.

Associated Content

Supplementary Information

Table S1. The DFT-calculated reaction and ionisation enthalpy, ΔH° (eV per functional unit), for various reactions of Mg atom with water molecules in aqueous environments

Table S2. Atomic charge (au) for Mg atom in various Mg compounds, as calculated via NPA method

Table S3. Estimation of rate constants from the DFT-calculations for kinetic model of the aqueous Mg electrochemical activity

Table S4-S6. Nernst-equations for competing electrochemical reactions on the Mg(0001), MgO(0001) and $Mg(OH)_2$(0001) surfaces in aqueous environments

Table S7. Metal-water and water-water interactions at the Mg(0001)/H_2O interface

Table S8. Tafel slope for multiple reaction pathways of HE in Mg surface

Figure S1. Optimised geometries at selected stationary points along the MEP for the water-splitting reaction on the Mg(0001) surface with H_2O under (a) H-up, (b) flat and (c) H-down configuration

Figure S2, S3. Optimised geometries at selected stationary points along the MEP for the Tafel and Heyrovksy *H recombinations on the Mg(0001) surface

Figure S4. The Heyrovsky reaction energy profile versus reaction pathway as obtained from the molecular dynamics calculation

Figure S5. Optimised geometries at selected stationary points along the MEP for Mg-dissolution on the Mg(0001) surface

Figure S6. Optimised geometries at selected stationary points along the MEP for *OH-dissociation (into subsurface O and *H) followed by the (a) Tafel and (b) Heyrovsky *H recombination

Figure S7. First-principles prediction of fractional surface coverage for free metallic sites, hydroxide-adsorption, oxygen-adsorption and hydrogen-adsorption as the functions of potential and pH

Figure S8. Reaction enthalpy of hydroxylation vs. surface coverage of *OH groups

Figure S9. Optimised geometries of Mg/H_2O interface with increasing number of water molecules with (a) dimer, (b) "cyclic" trimer, (c) "open" trimer, (d) "cyclic" tetramer, and (e) "open" tetramer configuration

Author Information

Corresponding Author

*Jodie A. Yuwono, Department of Materials Science and Engineering, Monash University, Melbourne, Australia.

jodie.yuwono@monash.edu

* Nikhil V. Medhekar, Department of Materials Science and Engineering, Monash University, Melbourne, Australia.

nikhil.medhekar@monash.edu

Funding Sources

J.A.Y received funding from the Monash International Postgraduate Scholarship (MIPRS), Monash Graduate Scholarship (MGS), Monash Study Away/ Travel Grant and Graduate Research International Travel Award (GRITA). N.B and N.V.M received funding from Australian Research Council DP Scheme (DP160103661). N.B. is supported by Woodside Energy.

Conflict of Interest

There are no conflicts to declare.

Acknowledgements

J.A.Y thanks Dr. Sebastian Thomas and Dr. Stephan Steinmann for helpful and constructive discussions. J.A.Y. and N.V.M gratefully acknowledge computational support from the Monash eResearch Centre, the Australian National Computing Infrastructure (NCI),

and the Pawsey Supercomputing Centre. N.V.M. and N.B. gratefully acknowledge the financial support from the Australian Research Council (DP160103661).

References

1. Emley, E. *Principles of magnesium technology*. (Pergamon Press, 1966).
2. Mordike, B. L. & Ebert, T. Magnesium Properties — applications — potential. *Mater. Sci. Eng. A* **302,** 37–45 (2001).
3. Mao, L. *et al.* A promising biodegradable magnesium alloy suitable for clinical vascular stent application. *Sci. Rep.* **7,** 1–12 (2017).
4. Zberg, B., Uggowitzer, P. J. & Löffler, J. F. MgZnCa glasses without clinically observable hydrogen evolution for biodegradable implants. *Nat. Mater.* **8,** 887–891 (2009).
5. Aurbach, D. *et al.* Prototype systems for rechargeable magnesium batteries. *Nature* **407,** 724–727 (2000).
6. Bucur, C. B., Gregory, T., Oliver, A. G. & Muldoon, J. Confession of a Magnesium Battery. *J. Phys. Chem. Lett.* **6,** 3578–3591 (2015).
7. Mohtadi, R. & Orimo, S. The renaissance of hydrides as energy materials. *Nat. Rev. Mater.* **2,** 1–16 (2016).
8. Schlapbach, L. & Züttel, A. Hydrogen storage materials for mobile applications. *Nature* **414,** 353–358 (2001).
9. Aguey-Zinsou, K. F. & Ares-Fernandez, J. R. Hydrogen in magnesium: new perspectives toward functional stores. *Energy Environ. Sci.* **3,** 526–543 (2010).
10. Abbott, T. B. Magnesium: Industrial and research developments over the last 15 years. *Corrosion* **71,** 120–127 (2015).
11. Frankel, G. S. Ready for the road. *Nat. Mater.* **14,** 1189–1190 (2015).
12. Beetz, W. On the development of hydrogen from the anode. *Philos. Mag.* **32,** 269–278 (1866).
13. Petty, R. L., Davidson, A. W. & Kleinberg, J. The anodic oxidation of magnesium metal : Evidence for the existence of unipositive magnesium. *J. Am. Chem. Soc.* **76,** 363–366 (1954).
14. Atrens, A. & Dietzel, W. The Negative Difference Effect and Unipositive Mg+. *Adv. Eng. Mater.* **9,** 292–297 (2007).
15. Kirkland, N. T., Williams, G. & Birbilis, N. Observations of the galvanostatic dissolution of pure magnesium. *Corros. Sci.* **65,** 5–9 (2012).
16. Kirkland, N. T., Williams, G. & Birbilis, N. Response to comments from Shi and Atrens on the paper "Observations of the galvanostatic dissolution of pure magnesium." *Corros. Sci.* **77,** 407–409 (2013).
17. Williams, G. & Mcmurray, H. N. Localized Corrosion of Magnesium in Chloride-Containing Technique. *J. Electrochem. Soc.* **155,** C340–C349 (2008).
18. Williams, G., Birbilis, N. & Mcmurray, H. N. The source of hydrogen evolved from a magnesium anode. *Electrochem. commun.* **36,** 1–5 (2013).
19. Williams, G., Dafydd, H. L. & Grace, R. The localised corrosion of Mg alloy AZ31 in chloride containing electrolyte studied by a scanning vibrating electrode technique. *Electrochim. Acta* **109,** 489–501 (2013).
20. Salleh, S. H., Thomas, S., Yuwono, J. A., Venkatesan, K. & Birbilis, N. Enhanced hydrogen evolution on Mg(OH)2 covered Mg surfaces. *Electrochim. Acta* **161,** 144–152 (2015).
21. Thomas, S. *et al.* On the effect of Fe concentration on Mg dissolution and activation studied using atomic emission spectroelectrochemistry and scanning electrochemical microscopy. *Electrochim. Acta* **210,** 271–284 (2016).
22. Swiatowska, J., Volovitch, P. & Ogle, K. The anodic dissolution of Mg in NaCl and Na2SO4 electrolytes by atomic emission spectroelectrochemistry. *Corros. Sci.* **52,** 2372–2378 (2010).
23. Birbilis, N. *et al.* Nuclear Microprobe Analysis for Determination of Element Enrichment Following Magnesium Dissolution. *ECS Electrochem. Lett.* **4,** C34–C37 (2015).
24. Liu, L. J. & Schlesinger, M. Corrosion of magnesium and its alloys. *Corros. Sci.* **51,** 1733–1737 (2009).
25. Birbilis, N., Shi, Z. & Atrens, A. Comments on the paper entitled "Observations of the galvanostatic dissolution of pure magnesium" by N. T. Kirkland , G. Williams and N. Birbilis. *Corros. Sci.* **77,** 403–406 (2013).
26. King, A. D., Birbilis, N. & Scully, J. R. Accurate electrochemical measurement of magnesium corrosion rates; A combined impedance, mass-loss and hydrogen collection study. *Electrochim. Acta* **121,** 394–406 (2014).
27. Frankel, G. S., Fajardo, S. & Lynch, B. M. Introductory lecture on corrosion chemistry: a focus on anodic hydrogen evolution on Al and Mg. *Faraday Discuss.* **180,** 11–33 (2015).
28. Fajardo, S. & Frankel, G. S. Effect of impurities on the enhanced catalytic activity for hydrogen evolution in high purity magnesium. *Electrochim. Acta* **165,** 255–267 (2015).

29. Williams, G., Dafydd, H. A. L., McMurray, H. N. & Birbilis, N. The influence of arsenic alloying on the localised corrosion behaviour of magnesium. *Electrochim. Acta* **219,** 401–411 (2016).

30. Eaves, D., Williams, G. & McMurray, H. N. Inhibition of self-corrosion in magnesium by poisoning hydrogen recombination on iron impurities. *Electrochim. Acta* **79,** 1–7 (2012).

31. Hoche, D. *et al.* The effect of iron re-deposition on the corrosion of impurity-containing magnesium. *Phys. Chem. Chem. Phys.* **18,** 1279–1291 (2016).

32. Lamaka, S. V., Hoche, D., Petrauskas, R. P., Blawert, C. & Zheludkevich, M. L. A new concept for corrosion inhibition of magnesium: Suppression of iron re-deposition. *Electrochem. commun.* **62,** 5–8 (2016).

33. Thomas, S., Medhekar, N. V., Frankel, G. S. & Birbilis, N. Corrosion mechanism and hydrogen evolution on Mg. *Curr. Opin. Solid State Mater. Sci.* **19,** 85–94 (2015).

34. Atrens, A. *et al.* Review of Recent Developments in the Field of Magnesium Corrosion. *Adv. Eng. Mater.* **17,** 400–453 (2015).

35. Chen, L. D., Nørskov, J. K., Luntz, A. C. & Page, S. Theoretical Limits to the Anode Potential in Aqueous Mg–Air Batteries. *J. Phys. Chem. C* **119,** 19660–19667 (2015).

36. Williams, K. S., Labukas, J. P., Rodriguez-Santiago, V. & Andzelm, J. W. First Principles Modeling of Water Dissociation on Mg(0001) and Development of a Mg Surface Pourbaix Diagram. *Corrosion* **71,** 209–223 (2015).

37. Tan, Q., Atrens, A., Mo, N. & Zhang, M. X. Oxidation of magnesium alloys at elevated temperatures in air: A review. *Corros. Sci.* **112,** 734–759 (2016).

38. Casey, E. J. & Bergeron, R. E. On the mechanism of the dissolution of magnesium in acidic salt solutions. *Can. J. Chem.* **31,** 849–867 (1953).

39. Hickling, A. The Anodic Behaviour of Metals. Part I. Platinum. *Trans. Faraday Soc.* **41,** 333–339 (1945).

40. Hickling, A. & Taylor, D. The Anodic Behaviour of Metals. Part V. Copper. *Trans. Faraday Soc.* **44,** 262–268 (1948).

41. Hickling, A. & Spice, J. E. The Anodic Behaviour of Metals. Part III. Nickel. *Trans. Faraday Soc.* **43,** 762–769 (1947).

42. Song, G. & Atrens, A. Corrosion mechanisms of magnesium alloys. *Adv. Eng. Mater.* **1,** 11–33 (1999).

43. Atrens, A., Liu, M., Abidin, N. I. Z. & Song, G. L. in *Corrosion of Magnesium Alloys* (ed. Song, G. L.) 117–165 (Woodhead Publishing Limited, 2011). doi:10.1533/9780857091413.2.117

44. Esmaily, M. *et al.* Fundamentals and advances in magnesium alloy corrosion. *Prog. Mater. Sci.* **89,** 92–193 (2017).

45. Atrens, A. D., Gentle, I. & Atrens, A. Possible dissolution pathways participating in the Mg corrosion reaction. *Corros. Sci.* **92,** 173–181 (2015).

46. Shi, Z., Jia, J. X. & Atrens, A. Galvanostatic anodic polarisation curves and galvanic corrosion of high purity Mg in 3.5% NaCl saturated with Mg(OH)2. *Corros. Sci.* **60,** 296–308 (2012).

47. Shi, Z. & Atrens, A. An innovative specimen configuration for the study of Mg corrosion. *Corros. Sci.* **53,** 226–246 (2011).

48. Robinson, J. L. & King, P. F. Electrochemical Behavior of the Magnesium Anode. *J. Electrochem. Soc.* **108,** 36–41 (1961).

49. King, P. F. Magnesium as a Passive Metal. *J. Electrochem. Soc.* **110,** 1113–1116 (1963).

50. King, P. F. The Role of the Anion in the Anodic Dissolution of Magnesium. *J. Electrochem. Soc.* **113,** 536–539 (1966).

51. Tunold, R., Holtan, H., Berge, M. B. H., Lasson, A. & Steen-Hansen, R. The corrosion of magnesium in aqueous solution containing chloride ions. *Corros. Sci.* **17,** 353–365 (1977).

52. Song, G., Atrens, A., John, D. St., Wu, X. & Nairn, J. The Anodic Dissolution of Magnesium and Sulphate Solutions in Chloride. *Corros. Sci.* **39,** 1981–2004 (1997).

53. Atrens, A., Song, G. L., Cao, F., Shi, Z. & Bowen, P. K. Advances in Mg corrosion and Research Suggestions. *J. Magnes. Alloy.* **1,** 177–200 (2013).

54. Song, G. & Atrens, A. Understanding Magnesium Corrosion — A Framework for Improved Alloy Performance. *Adv. Eng. Mater.* **5,** 837–858 (2003).

55. Song, G. Recent progress in corrosion and protection of magnesium alloys. *Adv. Eng. Mater.* **7,** 563–586 (2005).

56. Samaniego, A., Hurley, B. L. & Frankel, G. S. On the evidence for univalent Mg. *J. Electroanal. Chem.* **737,** 123–128 (2015).

57. Shi, Z., Cao, F., Song, G. L. & Atrens, A. Low apparent valence of Mg during corrosion. *Corros. Sci.* **88,** 434–443 (2014).

58. Thomas, S., Izquierdo, J., Birbilis, N. & Souto, R. M. Possibilities and limitations of scanning electrochemical microscopy of Mg and Mg alloys. *Corrosion* **71,** 171–183 (2015).

59. Song, G. L. in *Corrosion of Magnesium Alloys* (ed. Song, G. L.) 3–34 (Woodhead Publishing Limited, 2011). doi:http://dx.doi.org/10.1533/9780857091413.1.3

60. Chen, J., Dong, J., Wang, J., Han, E. & Ke, W. Effect of magnesium hydride on the corrosion behavior of an AZ91 magnesium alloy in sodium chloride solution. *Corros. Sci.* **50,** 3610–3614 (2008).

61. Xu, S., Dong, J. & Ke, W. Effect of Magnesium Hydride on the Corrosion Behavior of Pure Magnesium in 0.1 M NaCl Solution. *Int. J. Corros.* **2010,** 1–6 (2010).

62. Binns, W. J., Zargarzadah, F., Chen, J., Noël, J. J. & Dave, W. Physical and Electrochemical Evidence for the Role of a Mg Hydride Species in Mg Alloy Corrosion. *Corrosion* (2018).

63. Tefashe, U. M. *et al.* Local flux of hydrogen from magnesium alloy corrosion investigated by scanning electrochemical microscopy. *J. Electroanal. Chem.* **720–721,** 121–127 (2014).

64. Curioni, M. The behaviour of magnesium during free corrosion and potentiodynamic polarization investigated by real-time hydrogen measurement and optical imaging. *Electrochim. Acta* **120,** 284–292 (2014).

65. Curioni, M., Scenini, F., Monetta, T. & Bellucci, F. Correlation between electrochemical impedance measurements and corrosion rate of magnesium investigated by real-time hydrogen measurement and optical imaging. *Electrochim. Acta* **166,** 372–384 (2015).

66. Taheri, M. *et al.* Towards a Physical Description for the Origin of Enhanced Catalytic Activity of Corroding Magnesium Surfaces. *Electrochim. Acta* **116,** 396–403 (2014).

67. Danaie, M., Asmussen, R. M., Jakupi, P., Shoesmith, D. W. & Botton, G. A. The cathodic behaviour of Al-Mn precipitates during atmospheric and saline aqueous corrosion of a sand-cast AM50 alloy. *Corros. Sci.* **83,** 299–309 (2014).

68. Lysne, D., Thomas, S., Hurley, M. F. & Birbilis, N. On the Fe Enrichment during Anodic Polarization of Mg and Its Impact on Hydrogen Evolution. *J. Electrochem. Soc.* **162,** C396–C402 (2015).

69. Michailidou, E., McMurray, H. N. & Williams, G. Quantifying the Role of Transition Metal Electrodeposition in the Cathodic Activation of Corroding Magnesium. *J. Electrochem. Soc.* **165,** C195–C205 (2018).

70. Mercier, D., Swiatowska, J., Zanna, S., Seyeux, A. & Marcus, P. Role of Segregated Iron at Grain Boundaries on Mg Corrosion. *J. Electrochem. Soc.* **165,** C42–C49 (2018).

71. Yang, Y., Scenini, F. & Curioni, M. A study on magnesium corrosion by real-time imaging and electrochemical methods: relationship between local processes and hydrogen evolution. *Electrochim. Acta* **198,** 174–184 (2016).

72. Curioni, M., Torrescano-Alvarez, J. M., Yang, Y. F. & Scenini, F. Application of side-view imaging and real-time hydrogen measurement to the investigation of magnesium corrosion. *Corosion* **73,** 463–471 (2017).

73. Marco, I. & Van der Biest, O. Polarization measurements from a rotating disc electrode for characterization of magnesium corrosion. *Corros. Sci.* **102,** 384–393 (2016).

74. Cain, T. W., Gonzalez-Afanador, I., Birbilis, N. & Scully, J. R. The Role of Surface Films and Dissolution Products on the Negative Difference Effect for Magnesium: Comparison of Cl- versus Cl- Free Solutions. *J. Electrochem. Soc.* **164,** C300–C311 (2017).

75. Fajardo, S., Glover, C. F., Williams, G. & Frankel, G. S. The Source of Anodic Hydrogen Evolution on Ultra High Purity Magnesium. *Electrochim. Acta* **212,** 510–521 (2016).

76. Fajardo, S., Glover, C. F., Williams, G. & Frankel, G. S. The Evolution of Anodic Hydrogen on High Purity Magnesium in Acidic Buffer Solution. *Corrosion* **73,** 482–493 (2017).

77. Birbilis, N., King, A. D., Thomas, S., Frankel, G. S. & Scully, J. R. Evidence for enhanced catalytic activity of magnesium arising from anodic dissolution. *Electrochim. Acta* **132,** 277–283 (2014).

78. Zhang, W., Liu, Q., Chen, Y. & Wan, G. Anodic dissolution dictates the negative difference effect (NDE) of magnesium corrosion more in chemical pathway. *Mater. Lett.* **232,** 54–57 (2018).

79. Makar, G. L. & Kruger, J. Corrosion of magnesium. *Int. Mater. Rev.* **38,** 138–153 (1993).

80. Dauphin-Ducharme, P. & Mauzeroll, J. Surface Analytical Methods Applied to Magnesium Corrosion. *Anal. Chem.* **87,** 7499–7509 (2015).

81. Souto, R. M. *et al.* Spatially-resolved imaging of concentration distributions on corroding magnesium-based materials exposed to aqueous environments by SECM. *Electrochem. commun.* **26,** 25–28 (2013).

82. Skúlason, E. *et al.* Density functional theory calculations for the hydrogen evolution reaction in an electrochemical double layer on the Pt(111) electrode. *Phys. Chem. Chem. Phys.* **9,** 3241 (2007).

83. Rossmeisl, J., Skúlason, E., Björketun, M. E., Tripkovic, V. & Nørskov, J. K. Modeling the electrified solid-liquid interface. *Chem. Phys. Lett.* **466,** 68–71 (2008).

84. Skúlason, E. Modeling electrochemical reactions at the solid-liquid interface using density functional calculations. **51,** 1887–1896 (2015).

85. Sakong, S., Naderian, M., Mathew, K., Hennig, R. G. & Groß, A. Density functional theory study of the electrochemical interface between a Pt electrode and an aqueous electrolyte using an implicit solvent method. *J. Chem. Phys.* **142,** 234107 (2015).

86. Chan, K. & Nørskov, J. K. Electrochemical barriers made simple. *J. Phys. Chem. Lett.* **6,** 2663–2668 (2015).

87. Velikokhatnyi, O. I. & Kumta, P. N. First-principles studies on alloying and simplified thermodynamic aqueous chemical stability of calcium-, zinc-, aluminum-, yttrium- and iron-doped magnesium alloys. *Acta Biomater.* **6,** 1698–1704 (2010).

88. Williams, K. S., Rodriguez-Santiago, V. & Andzelm, J. W. Modeling reaction pathways for hydrogen evolution and water dissociation on magnesium. *Electrochim. Acta* **210,** 261–270 (2016).

89. Yuwono, J. A., Birbilis, N., Williams, K. S. & Medhekar, N. V. Electrochemical stability of Mg surfaces in an aqueous environment. *J. Phys. Chem. C* **120,** 26922–26933 (2016).

90. Taylor, C. D. A First-Principles Surface Reaction Kinetic Model for Hydrogen Evolution under Cathodic and Anodic Conditions on Magnesium. *J. Electrochem. Soc.* **163,** C602–C608 (2016).

91. Limmer, K. R., Williams, K. S., Labukas, J. P. & Andzelm, J. W. First Principles Modeling of Cathodic Reaction Thermodynamics in Dilute Magnesium Alloys. *Corrosion* **73,** 506–517 (2017).

92. Yuwono, J. A. *et al.* Aqueous electrochemical activity of the Mg surface : the role of group 14 and 15 microalloying elements. *J. Electrochem. Soc.* **164,** C918–C929 (2017).

93. Santucci, R. J., McMahon, M. E. & Scully, J. R. Utilization of chemical stability diagrams for improved understanding of electrochemical systems: evolution of solution chemistry towards equilibrium. *npj Mater. Degrad.* **2,** 1–9 (2018).

94. Ma, H. *et al.* First-principles modeling of anisotropic anodic dissolution of metals and alloys in corrosive environments. *Acta Mater.* **130,** 137–146 (2017).

95. Taylor, C. D., Li, S. & Samin, A. J. Oxidation versus salt-film formation: Competitive adsorption on a series of metals from first-principles. *Electrochim. Acta* **269,** 93–101 (2018).

96. Shao, Y. *et al.* Advances in methods and algorithms in a modern quantum chemistry program package. *Phys. Chem. Chem. Phys.* **8,** 3172–3191 (2006).

97. Hehre, W. J. *A Guide to Molecular Mechanics and Quantum Chemical Calculations*. (Wavefunction, Inc., 2003).

98. Hawkins, G. D., Cramer, C. J. & Truhlar, D. G. Universal Quantum Mechanical Model for Solvation Free Energies Based on Gas-Phase Geometries. *J. Phys. Chem. B* **102,** 3257–3271 (1998).

99. Reed, A. E., Weinstock, R. B. & Weinhold, F. Natural population analysis. *J. Chem. Phys.* **83,** 735–746 (1985).

100. Kresse, G. & Furthmüller, J. Efficient iterative schemes for ab initio total-energy calculations using a plane-wave basis set. *Phys. Rev. B* **54,** 11169–11186 (1996).

101. Kresse, G. & Furthmüller, J. Efficiency of ab-initio total energy calculations for metals and semiconductors using a plane-wave basis set. *Comput. Mater. Sci.* **6,** 15–50 (1996).

102. Perdew, J. P., Burke, K. & Ernzerhof, M. Generalized Gradient Approximation Made Simple. *Phys. Rev. Lett.* **77,** 3865–3868 (1996).

103. Blöchl, P. E. Projector augmented-wave method. *Phys. Rev. B* **50,** 17953–17979 (1994).

104. Kresse, G. From ultrasoft pseudopotentials to the projector augmented-wave method. *Phys. Rev. B* **59,** 1758–1775 (1999).

105. Carrasco, J., Hodgson, A. & Michaelides, A. A molecular perspective of water at metal interfaces. *Nat. Mater.* **11,** 667–674 (2012).

106. Henkelman, G., Uberuaga, B. P., Jónsson, H. & Henkelman, G. A climbing image nudged elastic band method for finding saddle points and minimum energy paths. *J. Chem. Phys.* **113,** 9901–9904 (2000).

107. Henkelman, G. & Jónsson, H. Improved tangent estimate in the nudged elastic band method for finding minimum energy paths and saddle points. *J. Chem. Phys.* **113,** 9978–9985 (2000).

108. Alsharaeh, E. H. Intracluster Ion Molecule Reactions Following the Generation of Mg+ Within Polar Clusters. *Int. J. Mol. Sci.* **12,** 9095–9107 (2011).

109. Atkins, P. W. & de Paula. *Physical Chemistry*. (Oxford University Press, 2010).

110. Pozzo, M. & Alfè, D. Hydrogen dissociation on Mg (0001) studied via quantum Monte Carlo calculations. *Phys. Rev. B* **78,** 245313 (2008).

111. Verdaguer, A., Sacha, G. M., Bluhm, H. & Salmeron, M. Molecular Structure of Water at Interfaces : Wetting at the Nanometer Scale. *Chem. Rev.* **106,** 1478–1510 (2006).

112. Hodgson, A. & Haq, S. Water adsorption and the wetting of metal surfaces. *Surf. Sci. Rep.* **64,** 381–451 (2009).

113. Björneholm, O. *et al.* Water at Interfaces. *Chem. Rev.* **116,** 7698–7726 (2016).

114. Revilla-Lopez, G. & Lopez, N. A unified study for water adsorption on metals: meaningful models from structural motifs. *Phys. Chem. Chem. Phys.* **16,** 18933–18940 (2014).

115. Henderson, M. The interaction of water with solid surfaces: fundamental aspects revisited. *Surf. Sci. Rep.* **46,** 1–308 (2002).

116. Bellarosa, L., Garcia-Muelas, R., Revilla-Lopez, G. & Lopez, N. Diversity at the Water−Metal Interface: Metal, Water Thickness, and Confinement Effects. *ACS Cent. Sci.* **2,** 109–116 (2016).

117. Gennero de Chialvo, M. R. & Chialvo, A. C. Hydrogen evolution reaction: Analysis of the Volmer-Heyrovsky-Tafel mechanism with a generalized adsorption model. *J. Electroanal. Chem.* **372,** 209–223 (1994).

118. Gennero de Chialvo, M. R. & Chialvo, A. C. Kinetics of hydrogen evolution reaction with Frumkin adsorption: re-examination of the Volmer–Heyrovsky and Volmer–Tafel routes. *Electrochim. Acta* **44,** 841–851 (1998).

119. Skúlason, E. *et al.* Modeling the Electrochemical Hydrogen Oxidation and Evolution Reactions on the Basis of Density Functional Theory Calculations. *J. Phys. Chem. C* **114,** 18182–18197 (2010).

120. Ishikawa, Y., Mateo, J. J., Tryk, D. A. & Cabrera, C. R. Direct molecular dynamics and density-functional theoretical study of the electrochemical hydrogen oxidation reaction and underpotential deposition of H on Pt(111). *J. Electroanal. Chem.* **607,** 37–46 (2007).

121. Taylor, C. D. The transition from metal–metal bonding to metal–solvent interactions during a dissolution event as assessed from electronic structure. *Chem. Phys. Lett.* **469,** 99–103 (2009).

122. Henkelman, G., Arnaldsson, A. & Jonsson, H. A fast and robust algorithm for Bader decomposition of charge density. *Comput. Mater. Sci.* **36,** 354–360 (2006).

123. Yu, M., Trinkle, D. R. & Introduction, I. Accurate and efficient algorithm for Bader charge integration. *J. Chem. Phys.* **134,** 64111 (2011).

124. Wachowicz, E. & Kiejna, A. Bulk and surface properties of hexagonal-close-packed Be and Mg. *J. Phys. Condens. Matter* **13,** 10767 (2001).

125. Bhambhani, P. & Munjal, N. Study of phase transition and cohesive energy in MgO. *J. Phys.* **377,** 12067 (2012).

126. Brady, M. P. *et al.* Film Breakdown and Nano-Porous Mg(OH)2 Formation from Corrosion of Magnesium Alloys in Salt Solutions. *J. Electrochem. Soc.* **162,** C140–C149 (2015).

127. Yao, H. B., Li, Y. & Wee, A. T. S. An XPS investigation of the oxidation r corrosion of melt-spun Mg. *Appl. Surf. Sci.* **158,** 112–119 (2000).

128. Santamaria, M., Quarto, F. Di, Zanna, S. & Marcus, P. Initial surface film on magnesium metal : A characterization by X-ray photoelectron spectroscopy (XPS) and photocurrent spectroscopy (PCS). *Electrochim. Acta* **53,** 1314–1324 (2007).

129. Taheri, M., Phillips, R. C., Kish, J. R. & Botton, G. A. Analysis of the surface film formed on Mg by exposure to water using a FIB cross-section and STEM-EDS. *Corros. Sci.* **59,** 222–228 (2012).

130. Unocic, K. A. *et al.* Transmission Electron Microscopy Study of Aqueous Film Formation and Evolution on Magnesium Alloys. *J. Electrochem. Soc.* **161,** C302–C311 (2014).

131. Nordlien, J. H., Ono, S., Masuko, N. & Nisancioglu, K. A TEM investigation of naturally formed oxide films on pure magnesium. *Corros. Sci.* **39,** 1397–1414 (1997).

132. Perrault, G. G. The potential-pH diagram of the magnesium-water system. *J. Electroanal. Chem. Interfacial Electrochem.* **51,** 107–119 (1974).

133. Lebouil, S., Gharbi, O., Volovitch, P. & Ogle, K. Mg dissolution in phosphate and chloride electrolytes: Insight into the mechanism of the negative difference effect. *Corrosion* **71,** 234–241 (2015).

134. Rossrucker, L. *et al.* The pH Dependence of Magnesium Dissolution and Hydrogen Evolution during Anodic Polarization. *J. Electrochem. Soc.* **162,** C333–C339 (2015).

135. Samaniego, A., Birbilis, N., Xia, X. & Frankel, G. S. Hydrogen Evolution During Anodic Polarization of Mg Alloyed with Li, Ca, or Fe. *Corrosion* **71,** 224–233 (2015).

136. Frankel, G. S., Samaniego, A. & Birbilis, N. Evolution of hydrogen at dissolving magnesium surfaces. *Corros. Sci.* **70,** 104–111 (2013).

137. Deshpande, K. B. Numerical modeling of micro-galvanic corrosion. *Electrochim. Acta* **56,** 1737–1745 (2011).

138. Rossrucker, L., Mayrhofer, K. J. J., Frankel, G. S. & Birbilis, N. Investigating the Real Time Dissolution of Mg Using Online Analysis by ICP-

MS. *J. Electrochem. Soc.* **161,** C115–C119 (2014).

139. Fajardo, S. & Frankel, G. S. Gravimetric Method for Hydrogen Evolution Measurements on Dissolving Magnesium. *J. Electrochem. Soc.* **162,** C693–C701 (2015).

140. Banjade, D. R., Porter, S. D., Mcmullan, B. M. & Harb, J. N. Hydrogen Evolution during the Corrosion of Galvanically Coupled Magnesium. *J. Electrochem. Soc.* **163,** C116–C123 (2016).

141. Feliu, S., Maffiotte, C., Samaniego, A., Galván, J. C. & Barranco, V. Effect of naturally formed oxide films and other variables in the early stages of Mg-alloy corrosion in NaCl solution. *Electrochim. Acta* **56,** 4554–4565 (2011).

142. Cain, T., Madden, S. B., Birbilis, N. & Scully, J. R. Evidence of the Enrichment of Transition Metal Elements on Corroding Magnesium Surfaces Using Rutherford Backscattering Spectrometry. *J. Electrochem. Soc.* **162,** C228–C237 (2015).

143. Fajardo, S. & Frankel, G. S. A kinetic model explaining the enhanced rates of hydrogen evolution on anodically polarized magnesium in aqueous environments. *Electrochem. commun.* **84,** 36–39 (2017).

144. Esmaily, M., Blücher, D. B., Svensson, J. E., Halvarsson, M. & Johansson, L. G. New insights into the corrosion of magnesium alloys — The role of aluminum. *Scr. Mater.* **115,** 91–95 (2016).

145. Schroder, E., Fasel, R. & Kiejna, A. O adsorption and incipient oxidation of the Mg(0001) surface. *Phys. Rev. B* **69,** 115431 (2004).

146. Francis, M. F. & Taylor, C. D. First-principles insights into the structure of the incipient magnesium oxide and its instability to decomposition: Oxygen chemisorption to Mg(0001) and thermodynamic stability. *Phys. Rev. B* **87,** 75450 (2013).

147. Hammer, B., Hansen, L. B. & Norskov, J. K. Improved adsorption energetics within density-functional theory using revised Perdew-Burke-Ernzerhof functionals. *Phys. Rev. B* **59,** 7413–7421 (1999).

148. Vassilev, P., Hartnig, C., Koper, M. T. M., Frechard, F. & Santen, R. A. Van. Ab initio molecular dynamics simulation of liquid water and water–vapor interface. *J. Chem. Phys.* **115,** 9815 (2001).

149. Vandevondele, J. *et al.* The influence of temperature and density functional models in ab initio molecular dynamics. *J. Chem. Phys.* **122,** 14515 (2005).

150. Grimme, S., Antony, J., Ehrlich, S. & Krieg, H. A consistent and accurate ab initio parametrization of density functional dispersion correction (DFT-D) for the 94 elements H-Pu. *J. Chem. Phys.* **132,** 154104 (2010).

151. Tonigold, K. & Groß, A. Dispersive Interactions in Water Bilayers at Metallic Surfaces : A Comparison of the PBE and RPBE Functional Including Semiempirical Dispersion Corrections. *J. Comput. Chem.* **33,** 695–701 (2012).

152. Carrasco, J., Klimeš, J. & Michaelides, A. The role of van der Waals forces in water adsorption on metals. *J. Chem. Phys.* **138,** 24708 (2013).

153. Lin, I., Seitsonen, A. P., Tavernelli, I. & Rothlisberger, U. Structure and Dynamics of Liquid Water from ab Initio Molecular Dynamics — Comparison of BLYP, PBE, and revPBE Density Functionals with and without van der Waals Corrections. *J. Chem. Theory Comput.* **8,** 3902–3910 (2012).

154. Forster-Tonigold, K. & Groß, A. Dispersion corrected RPBE studies of liquid water. *J. Chem. Phys.* **141,** 64501 (2014).

155. Santra, B. *et al.* On the accuracy of density-functional theory exchange-correlation functionals for H bonds in small water clusters. II. The water hexamer and van der Waals interactions. *J. Chem. Phys.* **129,** 194111 (2008).

156. Nezafati, M., Cho, K., Giri, A. & Kim, C. DFT study on the water molecule adsorption and the surface dissolution behavior of Mg alloys. *Mater. Chem. Phys.* **182,** 347–358 (2016).

157. Ibach, H. Vibration spectroscopy of water on stepped gold surfaces. *Surf. Sci.* **604,** 377–385 (2010).

158. Thiel, P. A. & Madey, T. E. The interaction of water with solid surfaces: Fundamental aspects. *Surf. Sci. Rep.* **7,** 211–385 (1987).

159. Cano, Z. P. *et al.* Physical characterization of cathodically-activated corrosion filaments on magnesium alloy AZ31B. *Corrosion* **71,** 146–159 (2015).

160. Liu, R. L., Thomas, S., Scully, J. R., Williams, G. & Birbilis, N. An Experimental Survey of the Cathodic Activation of Metals Including Mg, Sc, Gd, La, Al, Sn, Pb, and Ge in Dilute Chloride Solutions of Varying pH. *Corrosion* **73,** 494–505 (2017).

161. Surendralal, S., Todorova, M., Finnis, M. W. & Neugebauer, J. First-Principles Approach to Model Electrochemical Reactions : Understanding the Fundamental Mechanisms behind Mg Corrosion. *Phys. Rev. Lett.* **120,** 246801 (2018).

162. Ghali, E. in *Corrosion of Magnesium Alloys* (ed. Song, G. L.) 66–114 (Woodhead Publishing Limited, 2011). doi:http://dx.doi.org/10.1533/9780857091413.1.66

163. Turhan, M. C., Li, Q., Jha, H., Singer, R. F. & Virtanen, S. Corrosion behaviour of multiwall carbon nanotube/magnesium composites in 3.5% NaCl. *Electrochim. Acta* **56,** 7141–7148 (2011).

164. Qiao, Z., Shi, Z., Hort, N., Abidin, N. I. Z. & Atrens, A. Corrosion behaviour of a nominally high purity Mg ingot produced by permanent mould direct chill casting. *Corros. Sci.* **61,** 185–207 (2012).

165. Cao, F. *et al.* Corrosion of ultra-high-purity Mg in 3.5% NaCl solution saturated with Mg(OH)2. *Corros. Sci.* **75,** 78–99 (2013).

166. Lim, T. S., Ryu, H. S. & Hong, S. Electrochemical corrosion properties of CeO2 -containing coatings on AZ31 magnesium alloys prepared by plasma electrolytic oxidation. *Corros. Sci.* **62,** 104–111 (2012).

167. Gusieva, K., Davies, C. H. J., Scully, J. R. & Birbilis, N. Corrosion of magnesium alloys: the role of alloying. *Int. Mater. Rev.* **60,** 169–194 (2014).

168. Xu, W. *et al.* A high-specific-strength and corrosion-resistant magnesium alloy. *Nat. Mater.* **14,** 1229–1236 (2015).

169. Kang, H. *et al.* Multi-functional magnesium alloys containing interstitial oxygen atoms. *Sci. Rep.* **6,** 1–8 (2016).

170. Zhang, X. *et al.* Mitigation of Corrosion on Magnesium Alloy by Predesigned Surface Corrosion. *Sci. Rep.* **5,** 1–11 (2015).

171. Wu, G., Ibrahim, J. M. & Chu, P. K. Surface design of biodegradable magnesium alloys — A review. *Surf. Coat. Technol.* **233,** 2–12 (2013).

172. Martin, W. C. & Zalubas, R. Energy levels of magnesium, Mg I through Mg XII. *J. Phys. Chem. Ref. Data* **9,** 1–58 (1980).

Table 1. The DFT-calculated reaction enthalpy for Mg complex in aqueous environments

Structure	Reaction enthalpy - $\Delta H°_r$ (eV per functional unit)				
	0 → +1	0 → +2	+1 → +1	+1 → +2	+2 → +2
Mg-6H_2O	0.473	15.502	-7.255	7.775	-60.867
Mg-4H_2O-2OH	1.401	13.690	-6.326	5.963	-62.679

Note:

$\Delta H°_{r_{Mg-6H_2O\,(0\rightarrow+1)}} = H°_{Mg-6H_2O^+} - H°_{Mg} - 6\,H°_{H_2O}$

$\Delta H°_{r_{Mg-6H_2O\,(+1\rightarrow+1)}} = H°_{Mg-6H_2O^+} - H°_{Mg^+} - 6\,H°_{H_2O}$

$\Delta H°_{r_{Mg-6H_2O\,(+1\rightarrow+2)}} = H°_{Mg-6H_2O^{2+}} - H°_{Mg^+} - 6\,H°_{H_2O}$

Table 2. The DFT-calculated reaction enthalpy for the Mg surfaces transformation during the interaction with water molecules in aqueous environments

Electrochemical Reaction	ΔH_r (eV per H_2O)
$Mg + 3H_2O \rightarrow Mg^*O_3 + 3H_2$	-2.76
$Mg + 6H_2O \rightarrow Mg^*O_6 + 6H_2$	-2.67
$Mg + 4H_2O \rightarrow Mg^*(OH)_4 + 2H_2$	-1.67
$Mg + 8H_2O \rightarrow Mg^*O_4(OH)_4 + 6H_2$	-1.90
$Mg^*O_3 + 5H_2O \rightarrow Mg^*O_4(OH)_4 + 3H_2$	-2.32
$Mg^*O_3 + H_2O + H_2 \rightarrow Mg^*(OH)_4$	1.58
$Mg^*O_3 + 3H_2O \rightarrow Mg^*O_6 + 3H_2$	-2.59
$Mg^*O_6 + 2H_2O \rightarrow Mg^*O_4(OH)_4$	3.93

Table 3. Comparison of Tafel slope calculated in this study and reported in the literature

Material	Tafel Determination Method	OCP (V vs. SHE)	β_a (mV dec^{-1})	β_c (mV dec^{-1})	pH	Electrolyte	Ref.
Pure Mg	Simulation Tafel extrapolation	-1.50	127.65	346.42	3	H_2O	This study
Pure Mg	Simulation Tafel extrapolation	-1.65	146.13	170.82	7	H_2O	This study
Pure Mg	Simulation Tafel extrapolation	-1.80	141.61	135.72	11	H_2O	This study
CP Mg	Experimental Tafel extrapolation	-1.38	31.0	186.0	-	NaCl	[163]
CP Mg	Experimental Tafel extrapolation	-1.31	150.0	315.0	5.4	NaCl	[26]
CP Mg	Experimental Tafel extrapolation	-1.29	58.0	246.0	-	NaCl	[163]
CP Mg	Experimental Levenberg-Marquardt	-1.35	54.5	334.5	-	NaCl	[164]
CP Mg	Experimental Levenberg-Marquardt	-1.35	50.0	304.7	-	NaCl	[164]
CP Mg	Experimental Levenberg-Marquardt	-1.31	82.0	260.0	-	NaCl	[165]
CP Mg	Experimental Levenberg-Marquardt	-1.06	31.5	183.0	-	NaCl	[165]
CP Mg	Experimental Tafel extrapolation	-1.31	27.0	168.0	-	NaCl	[166]

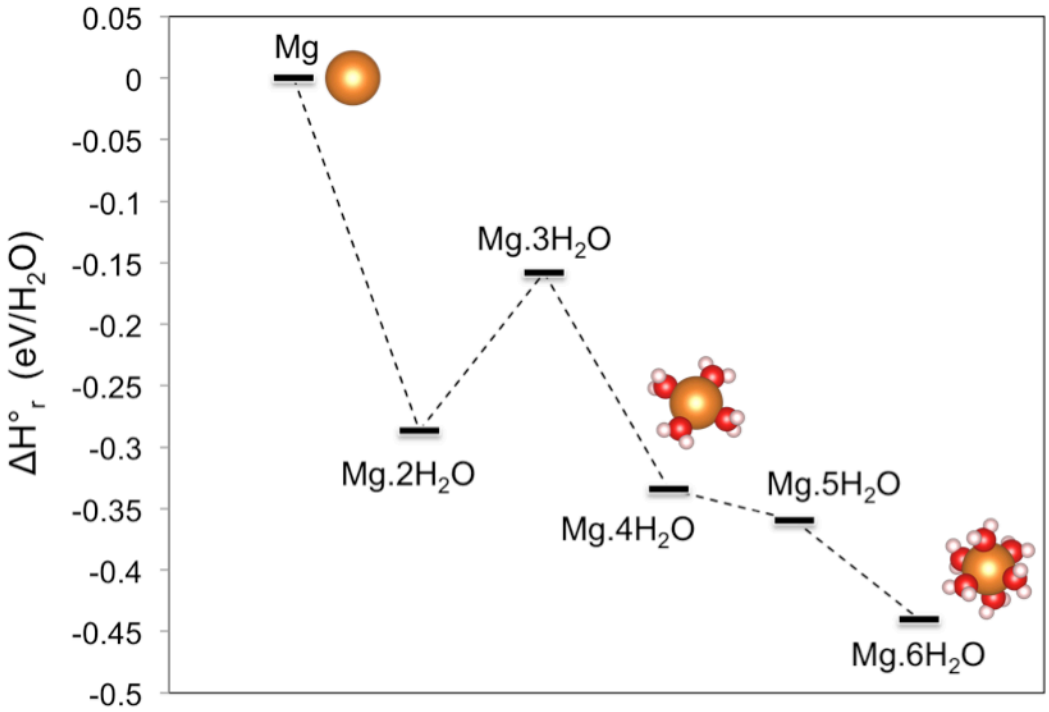

Figure 1. Reaction enthalpy of Mg atom with water molecules forming $Mg.(H_2O)_x$ complexes in aqueous environments

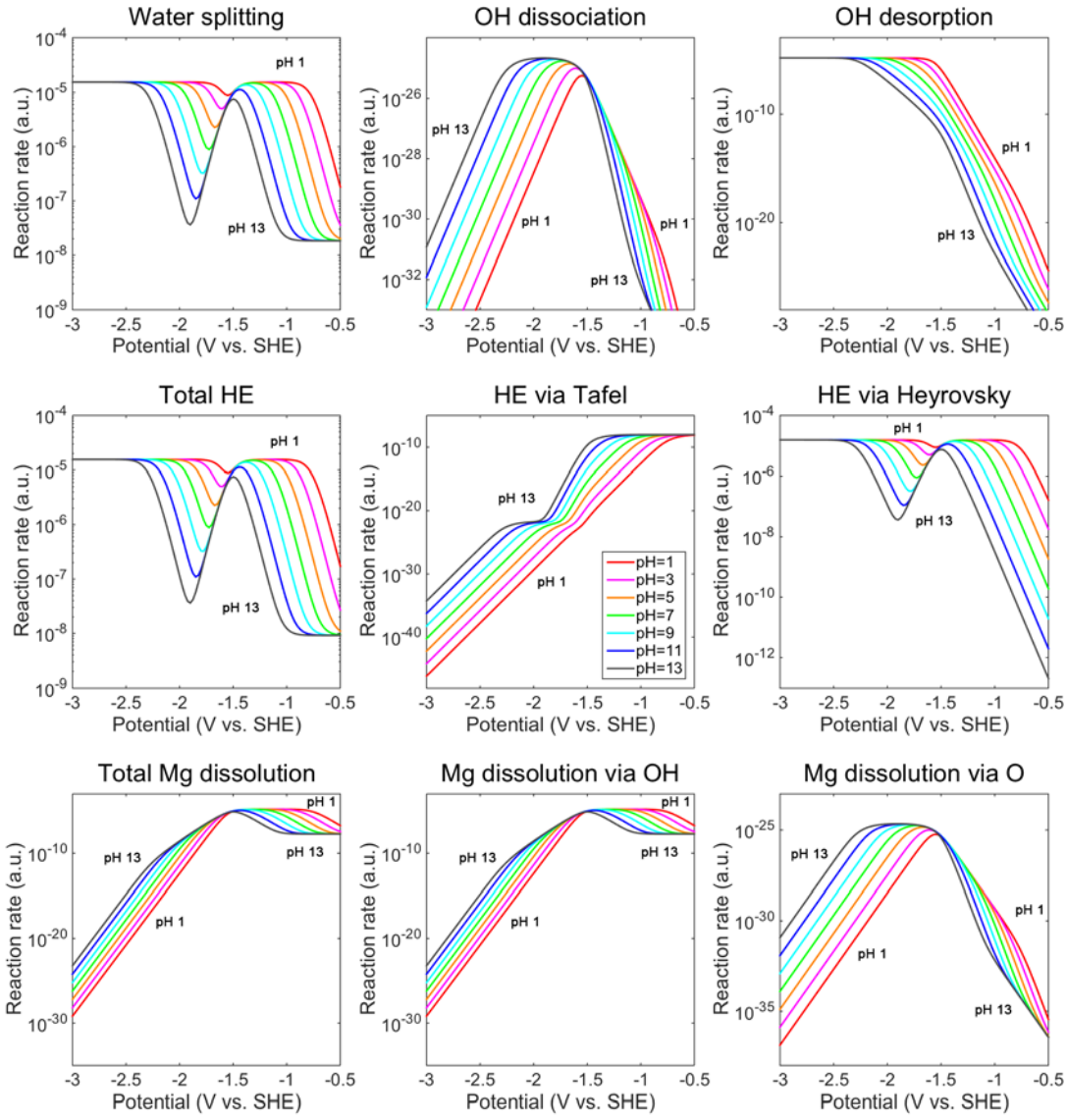

Figure 2. Kinetic profiles of various elementary reactions on the Mg(0001) surface as the functions of potential and pH

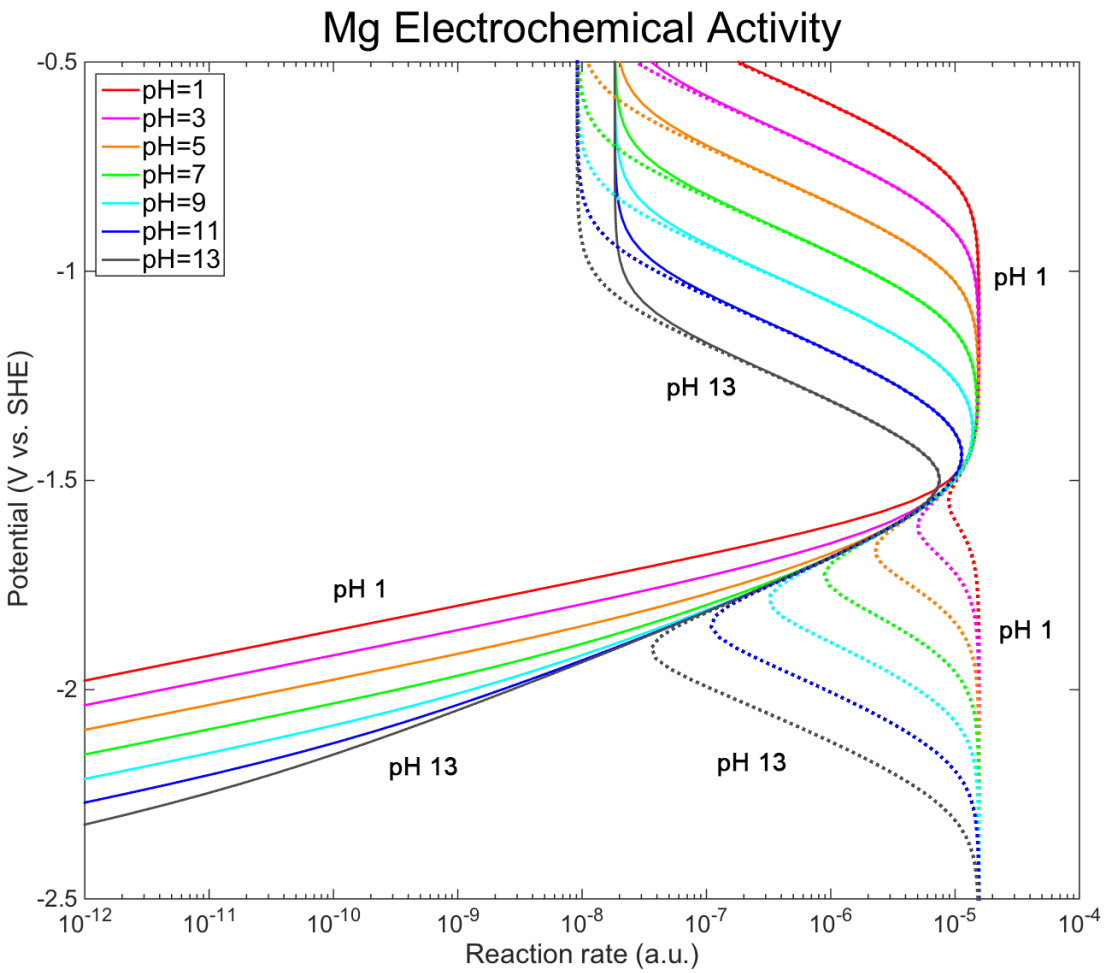

Figure 3. The DFT-calculated polarisation curves for Mg electrochemical activity in aqueous environments at different pH values, showing cathodic (water-splitting/ HE – dotted lines) and anodic (Mg-dissolution – solid lines) branches

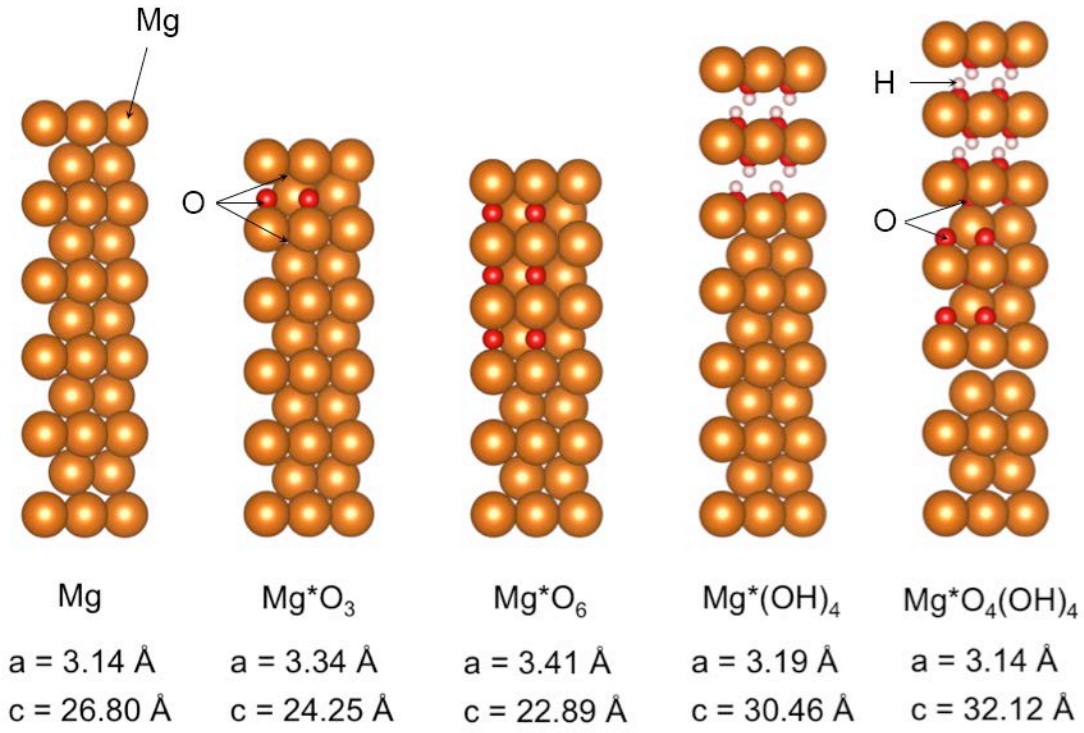

Figure 4. Optimised geometries of (2x2x1) Mg supercell used for the transformation study of Mg surface forming an oxidation film of MgO, $Mg(OH)_2$ and $MgO/Mg(OH)_2$

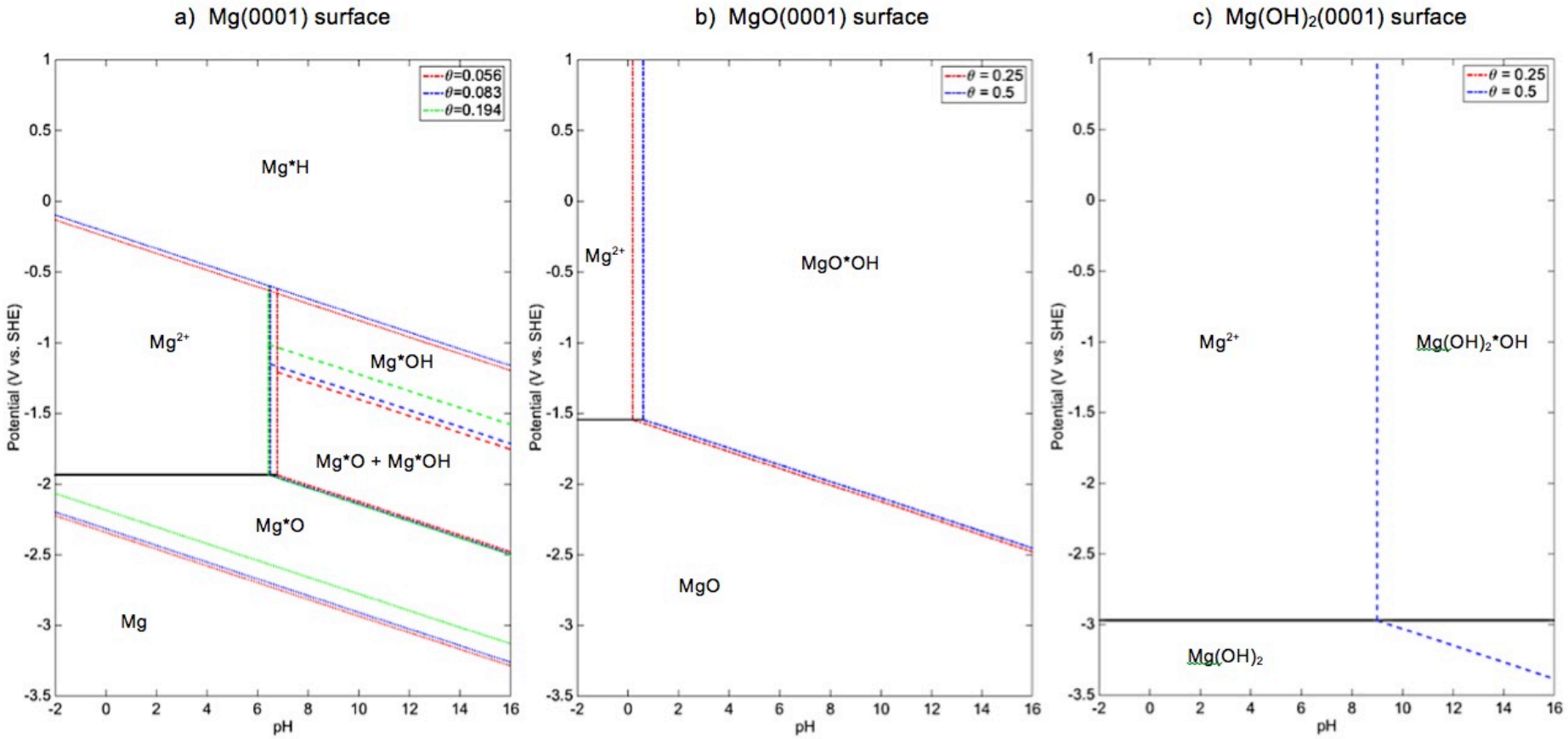

Figure 5. The DFT-calculated Pourbaix-diagrams of (0001) surfaces of hcp Mg (a), MgO (b) and $Mg(OH)_2$ (c) in aqueous environments

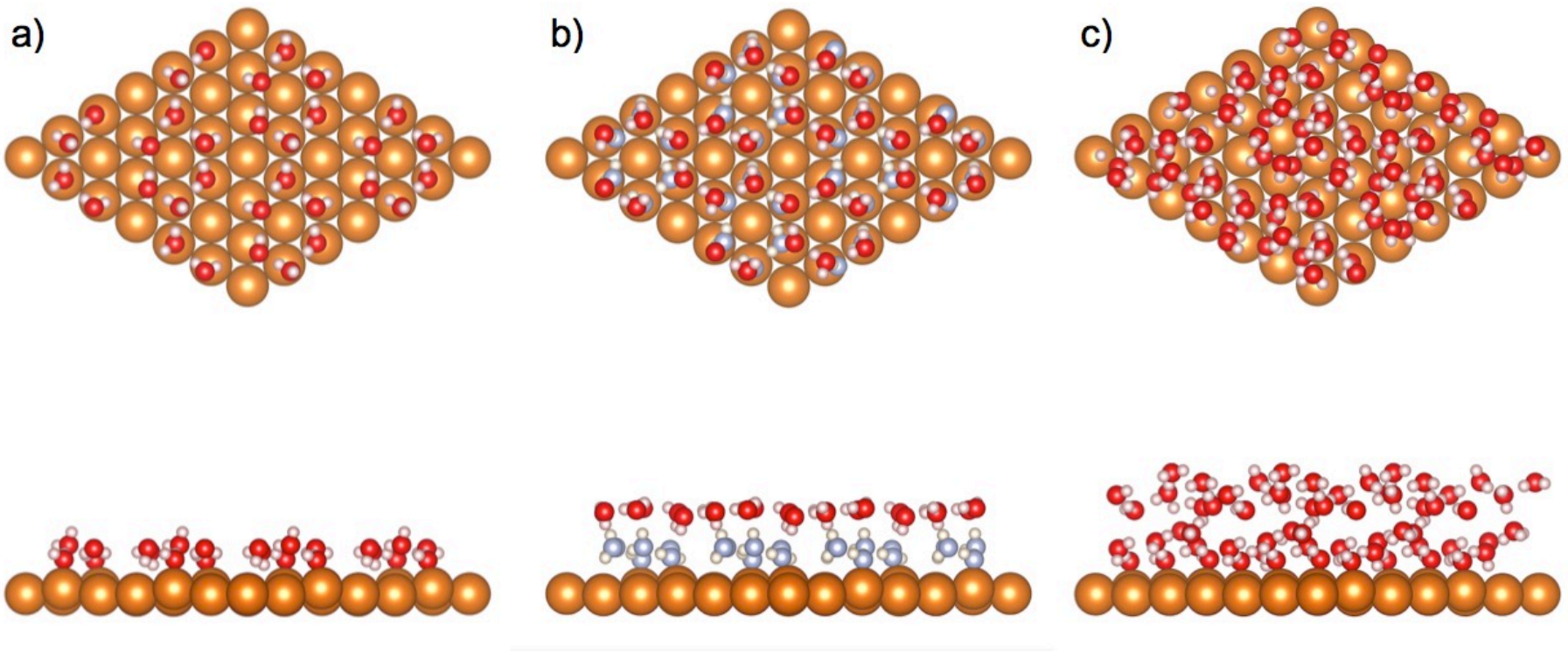

Figure 6. Top and side view of the optimised geometries for the water EDL on the Mg(0001) surface with (a) single, (b) double and (c) triple water bilayer structure

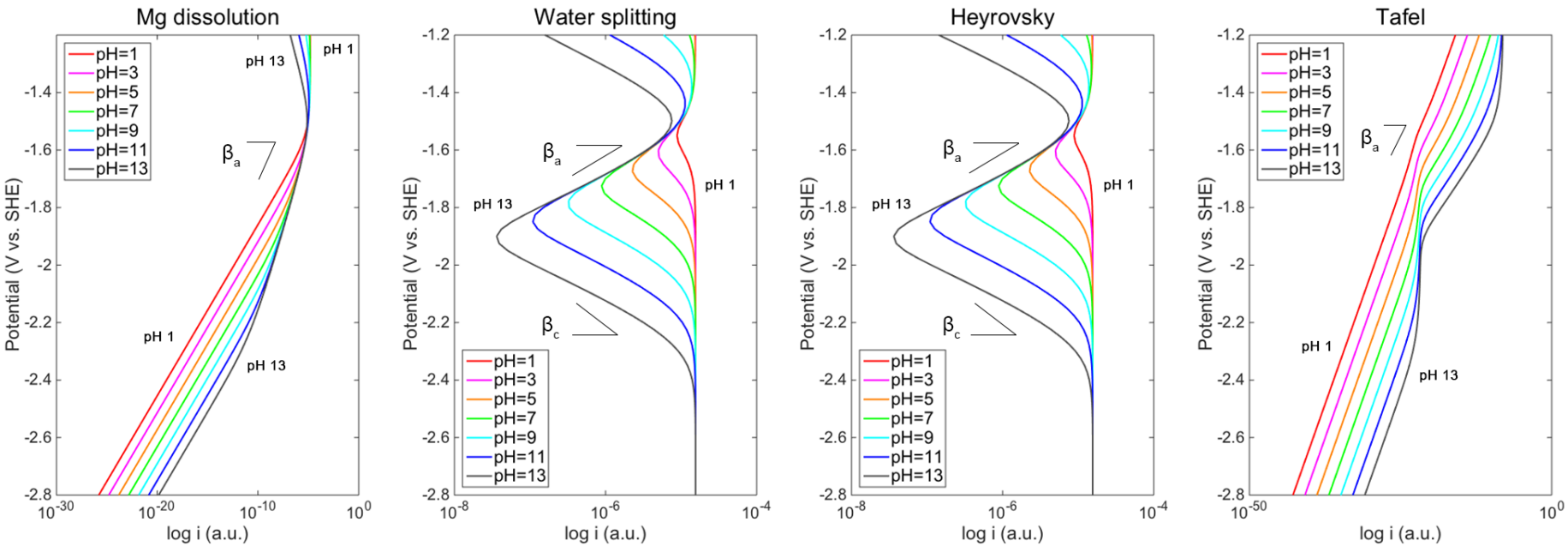

Figure 7. Cathodic and anodic branches determined from reactions 4, 5 and 8 with their corresponding Tafel slopes (β) are listed in Table S8

Graphical Abstract

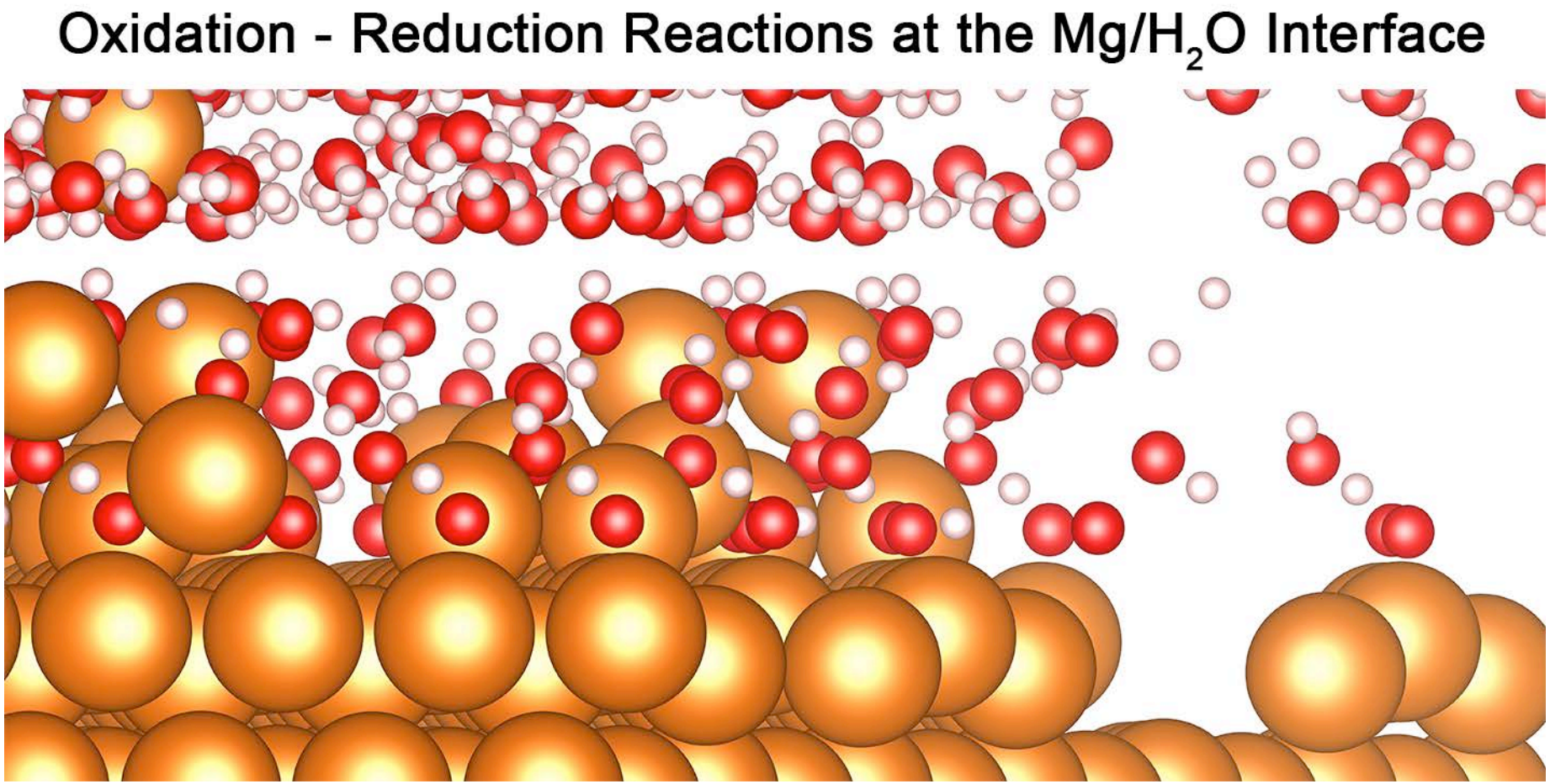

Supplementary Information for "Aqueous Electrochemistry of the Magnesium Surface: Thermodynamic and Kinetic Profiles"

Jodie Adrian Yuwono[1,*], Nick Birbilis[1], Christopher D. Taylor[2,3], Kristen S. Williams[4], Adib J. Samin[5], Nikhil V. Medhekar[1,*]

[1] Department of Materials Science and Engineering, Monash University, Clayton VIC 3800, Australia

[2] Fontana Corrosion Center, Department of Materials Science and Engineering, The Ohio State University, Columbus OH 43210, USA

[3] Strategic Research and Innovation, DNV GL, Dublin OH 43017, USA

[4] Boeing Research and Technology, Huntsville AL 35824, USA

[5] Los Alamos National Laboratory, Los Alamos NM 87545, USA

*Corresponding author: jodie.yuwono@monash.edu, nikhil.medhekar@monash.edu

Table S1. The DFT-calculated reaction and ionisation enthalpy, ΔH° (eV per functional unit), for various reactions of Mg atom with water molecules in aqueous environments

Structure	ΔH°_r	$\Delta H^\circ_{i\,(0 \rightarrow +1)}$	$\Delta H^\circ_{i\,(+1 \rightarrow +2)}$	$\Delta H^\circ_{i\,(+2 \rightarrow +3)}$
Mg	-	7.727 (7.646)[172]	68.642 (15.035)[172]	96.681 (80.143)[172]
Mg-2H_2O	-0.287	40.916	-	-
Mg-3H_2O	-0.158	4.169	-	-
Mg-4H_2O	-0.334	3.707	-	-
Mg-5H_2O	-0.360	3.270	14.586	-
Mg-6H_2O	-0.440	3.114	15.029	-
Mg-OH-H	-1.023	9.909	15.839	-
Mg-2OH	-0.962	9.709	-	-
Mg-4H_2O-2OH	-1.058	7.912	12.289	-
Mg-4H_2O-O	-0.300	4.617	11.862	-
Mg-O	2.814	7.665	16.044	-
Mg-2H	3.060	9.592	16.594	

Table S2. Atomic charge (au) for Mg atom in various Mg compounds, as calculated via NPA method

Structure	Neutral state	Positive charged-state	
	0	+1	+2
Mg	0	1	2
Mg-2H_2O	0.07	0.96	-
Mg-3H_2O	0.24	1.00	-
Mg-4H_2O	0.22	1.01	-
Mg-5H_2O	0.59	1.21	1.77
Mg-6H_2O	0.53	1.21	1.15
Mg-OH-H	1.54	1.61	1.83
Mg-2OH	1.73	1.85	-
Mg-4H_2O-2OH	1.72	1.76	1.78
Mg-2H	1.30	1.27	1.73
Mg-O	1.11	1.64	1.90
Mg-4H_2O-O	1.53	1.70	1.78

Table S3. Estimation of rate constants from the DFT-calculations for kinetic model of the aqueous Mg electrochemical activity

Reaction No.	A	E_a	U_0
[9]	1.0×10^{13} *	1.06	-
[10]	1.0×10^{14} **	1.31	-
[11]	1.0×10^{13} *	1.90	-0.83
[12]	1.0×10^{13} *	1.51	-2.38
[13]	1.0×10^{13} *	1.08	-0.83
[14]	1.0×10^{13} *	2.24	-
[15]	1.0×10^{13} *	1.51	-2.83

Note: The values of * and ** are obtained from references 109 and 110, respectively.

Table S4. Nernst-equations for competing electrochemical reactions on the Mg(0001) surface in aqueous environments

Reaction No.	Surface coverage, θ (ML)	Nernst-equation
[22]	0.056	E = -1.534 – 0.0591 pH
	0.083	E = -1.550 – 0.0591 pH
	0.194	E = -1554 – 0.0591 pH
[23]	0.056	E = -2.342 – 0.0591 pH
	0.083	E = -2.317 – 0.0591 pH
	0.194	E = -2.186 – 0.0591 pH
[24]	0.056	E = -0.808 – 0.0591 pH
	0.083	E = -0.767 – 0.0591 pH
	0.194	E = -0.632 – 0.0591 pH
[25]	0.056	$\log[Mg^{2+}] = 12.99 - 2\ pH$
	0.083	$\log[Mg^{2+}] = 12.87 - 2\ pH$
	0.194	$\log[Mg^{2+}] = 12.63 - 2\ pH$
[26]	0.056	$\log[Mg^{2+}] = -13.80 - 2\ pH$
	0.083	$\log[Mg^{2+}] = -12.96 - 2\ pH$
	0.194	$\log[Mg^{2+}] = -8.52 - 2\ pH$
[27]	0	$E = -1.934 + 0.0295 \log[Mg^{2+}]$
[28]	0.056	E = -0.250 – 0.0591 pH
	0.083	E = -0.216 – 0.0591 pH

Table S5. Nernst-equations for competing electrochemical reactions on the MgO(0001) surface in aqueous environments

Reaction No.	Surface coverage, θ (ML)	Nernst-equation
[29]	0.25	$E = -1.533 - 0.0591\ pH$
	0.50	$E = -1.508 - 0.0591\ pH$
[30]	0.25	$\log[Mg^{2+}] = 0.35 - 2\ pH$
	0.50	$\log[Mg^{2+}] = 1.19 - 2\ pH$
[31]	0	$E = -1.543 + 0.0295 \log[Mg^{2+}]$

Table S6. Nernst-equations for competing electrochemical reactions on the $Mg(OH)_2(0001)$ surface in aqueous environments

Reaction No.	Surface coverage, θ (ML)	Nernst-equation
[32]	0.25	E = -1.206 – 0.0591 pH
	0.50	E = -2.440 – 0.0591 pH
[33]	0.25	$\log[Mg^{2+}]$ = 59.73 – 2 pH
	0.50	$\log[Mg^{2+}]$ = 17.97 – 2 pH
[34]	0	E = -2.971+ 0.0295 $\log[Mg^{2+}]$

Table S7. Metal-water and water-water interactions at the Mg(0001)/H_2O interface

Structure	E_{Mg-H_2O} (eV per H_2O)	$E_{H_2O-H_2O}$ (eV per H_2O)
monomer	-0.41	-
dimer	-0.48	-0.09
"open" trimer	-0.51	-0.15
"cyclic" trimer	-0.45	-
"open" tetramer	-0.51	-
"cyclic" tetramer	-0.54	-0.16
single bilayer	-0.53	-0.26
double bilayer	-0.53	-0.42
triple bilayer	-0.55	-0.43

Table S8. Tafel slope for multiple reaction pathways of HE in Mg surface

pH	Open circuit potential (V vs. SHE)	Mg-dissolution	Water-splitting		Hydrogen-evolution		
			Volmer		Heyrovsky		Tafel
		β_a (mV dec^{-1})	β_c (mV dec^{-1})	β_a (mV dec^{-1})	β_c (mV dec^{-1})	β_a (mV dec^{-1})	β_a (mV dec^{-1})
3	-1.50	127.65	346.42	388.45	346.42	388.45	45.56
7	-1.65	146.13	170.82	194.37	170.82	194.37	36.91
11	-1.80	146.61	135.72	137.07	135.72	137.07	31.86

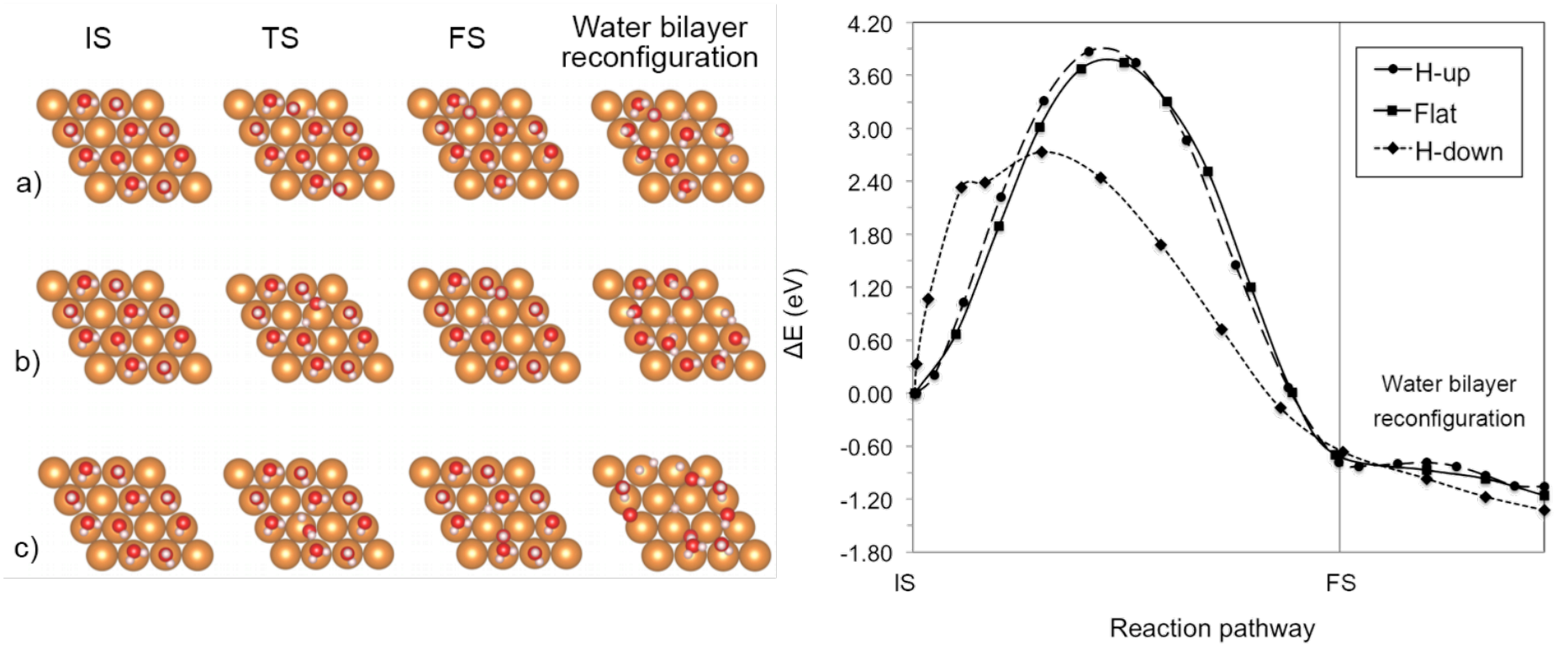

Figure S1. Optimised geometries at selected stationary points along the MEP for the water-splitting reaction on the Mg(0001) surface with H_2O under (a) H-up, (b) flat and (c) H-down configuration

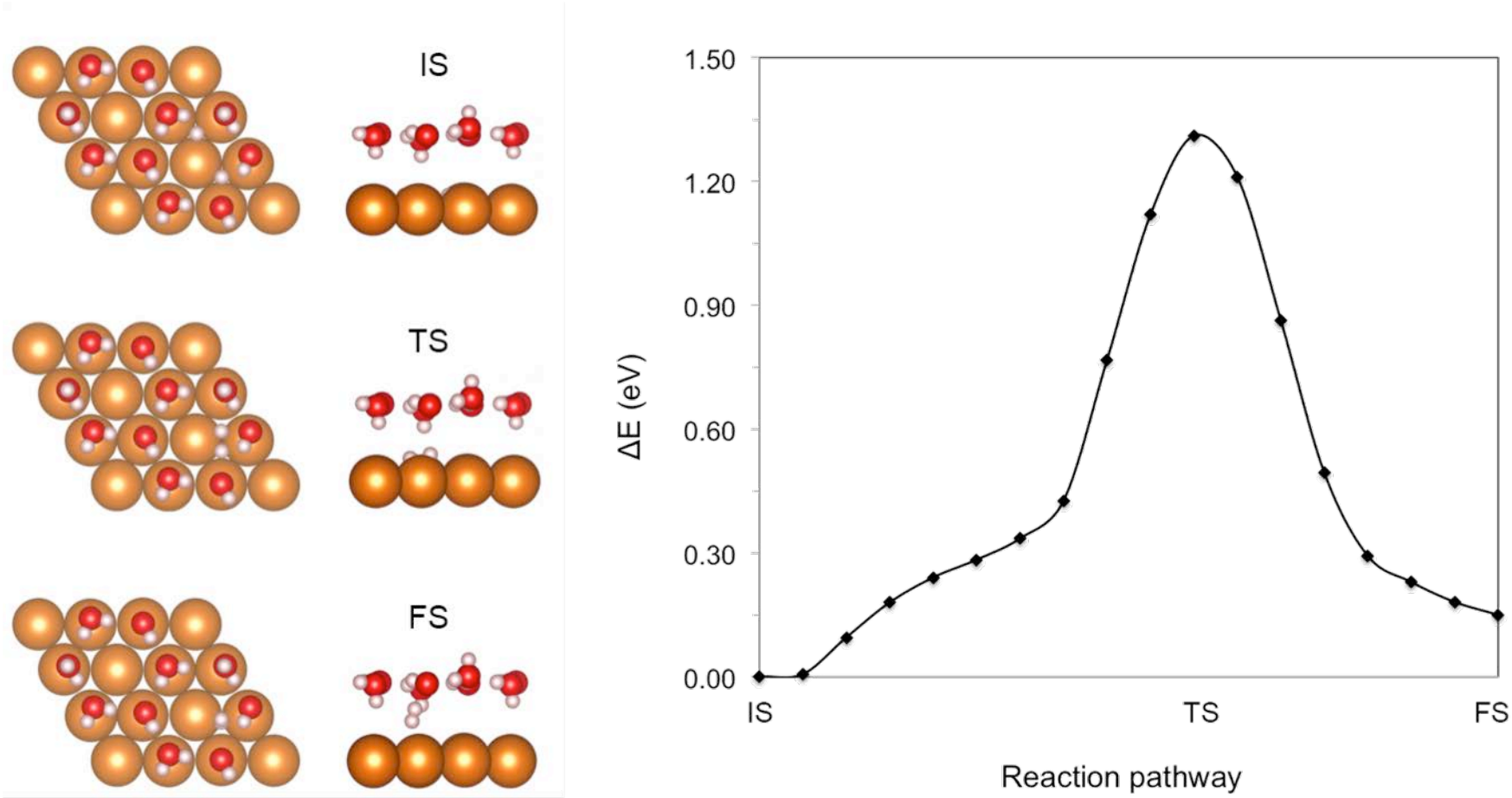

Figure S2. Optimised geometries at selected stationary points along the MEP for the Tafel *H recombination on the Mg(0001) surface

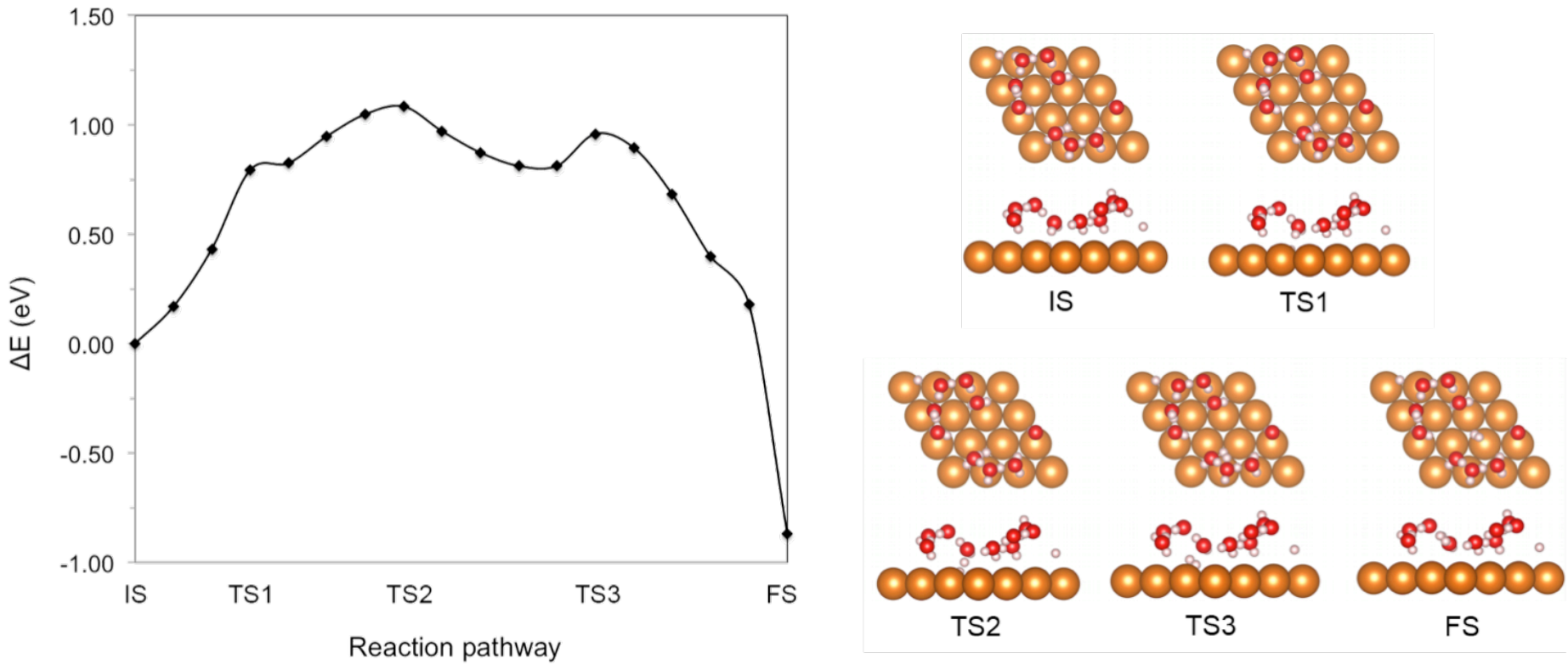

Figure S3. Optimised geometries at selected stationary points along the MEP for the Heyrovsky *H recombination on the Mg(0001) surface

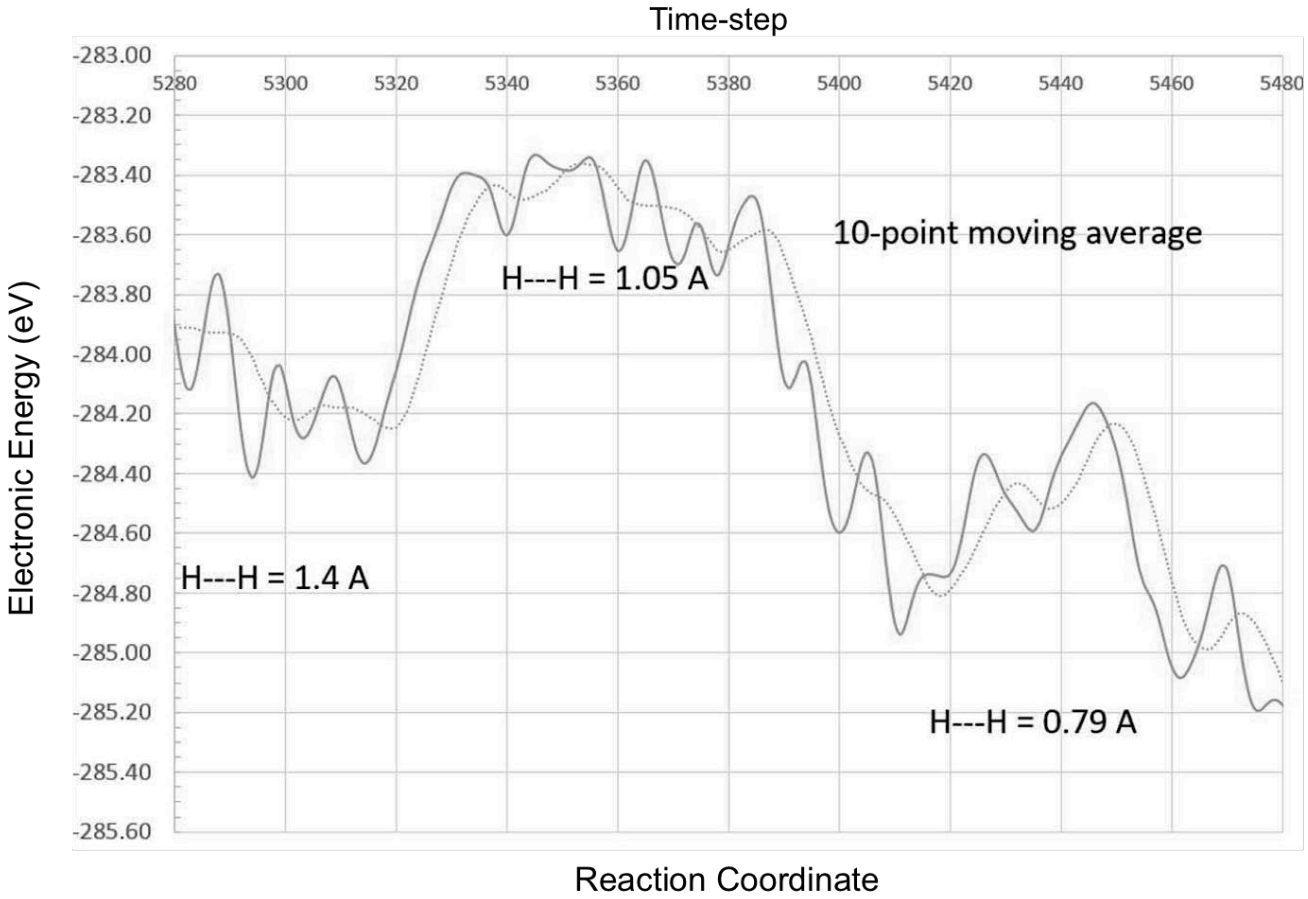

Figure S4. The Heyrovsky reaction energy profile versus reaction pathway as obtained from the molecular dynamics calculation

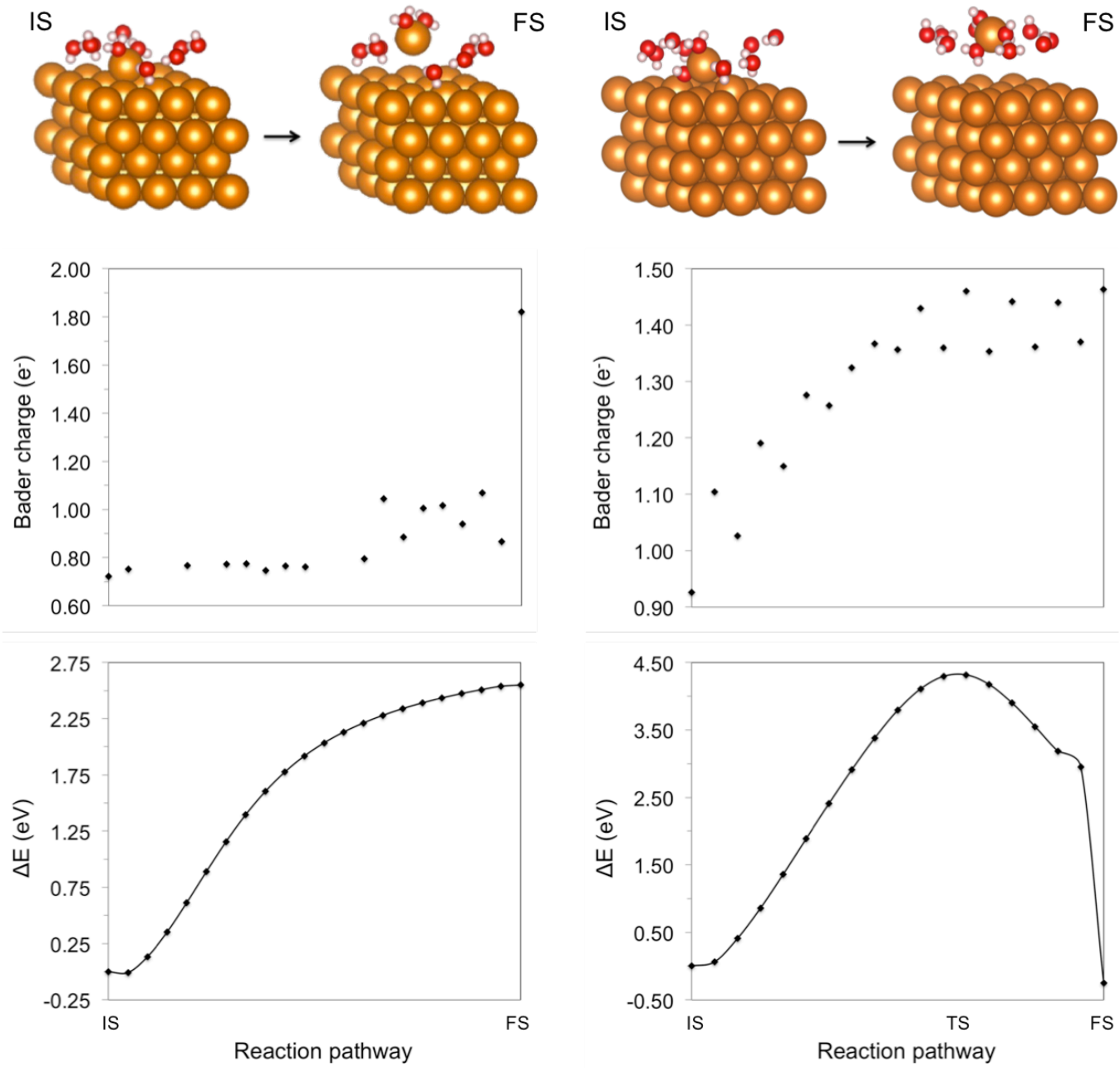

Figure S5. Optimised geometries at selected stationary points along the MEP for Mg-dissolution on the Mg(0001) surface

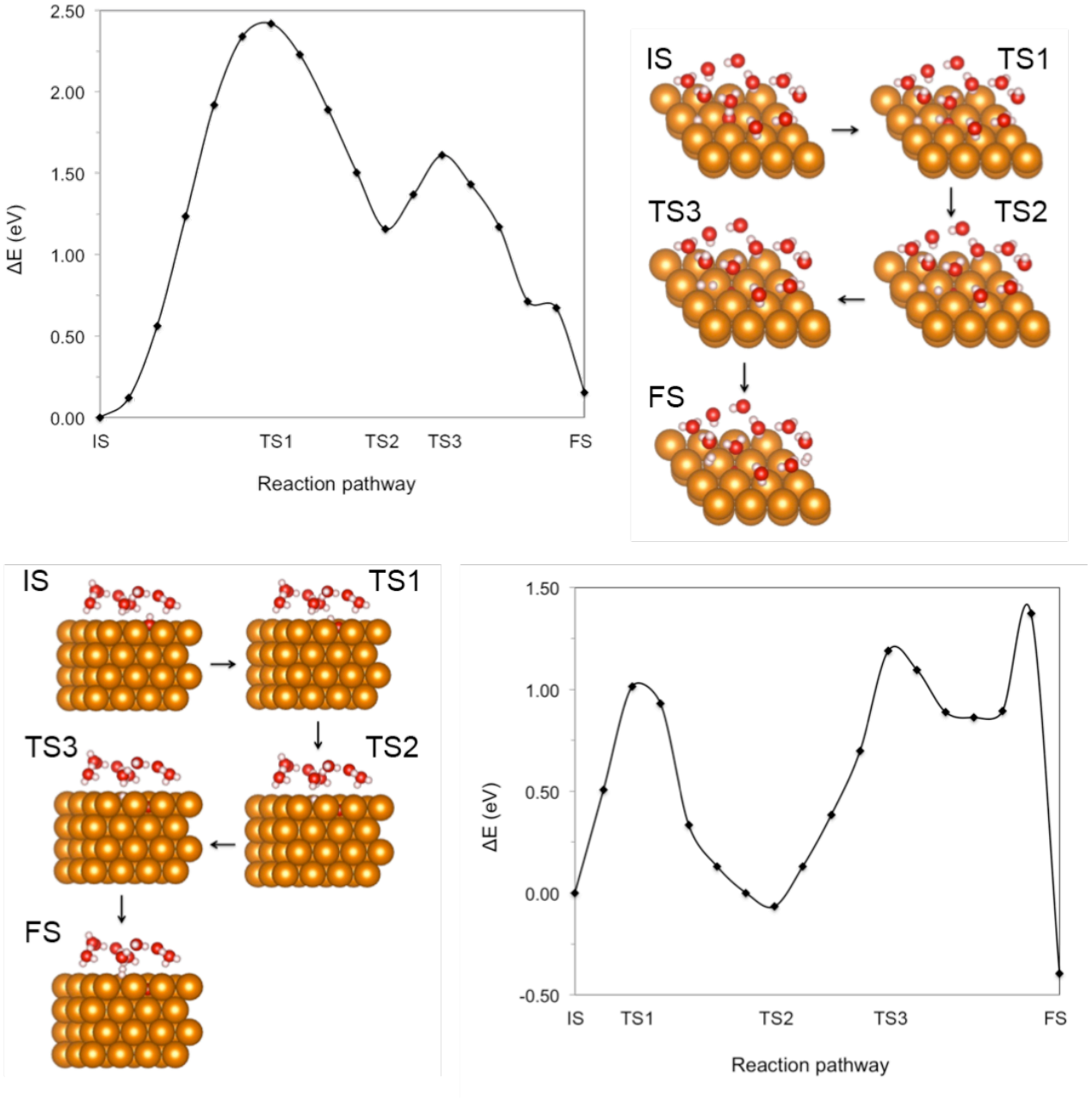

Figure S6. Optimised geometries at selected stationary points along the MEP for *OH-dissociation (into subsurface O and *H) followed by the (a) Tafel and (b) Heyrovsky *H recombination

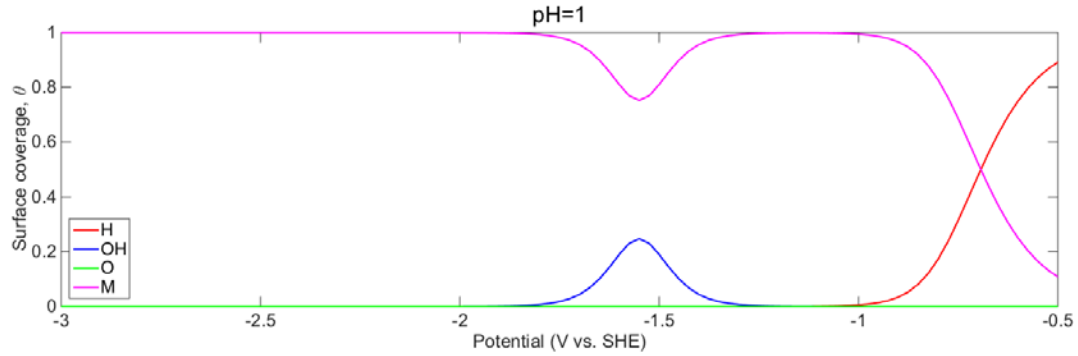
pH=1
Surface coverage, θ
H
OH
O
M
Potential (V vs. SHE)

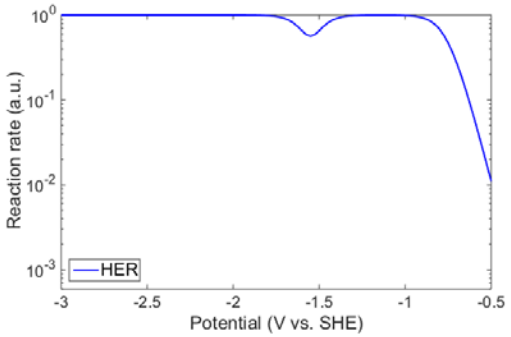
Reaction rate (a.u.)
HER
Potential (V vs. SHE)

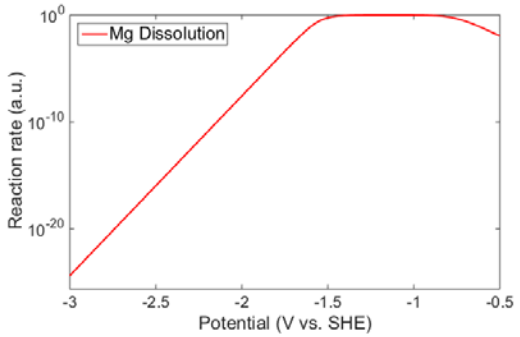
Reaction rate (a.u.)
Mg Dissolution
Potential (V vs. SHE)

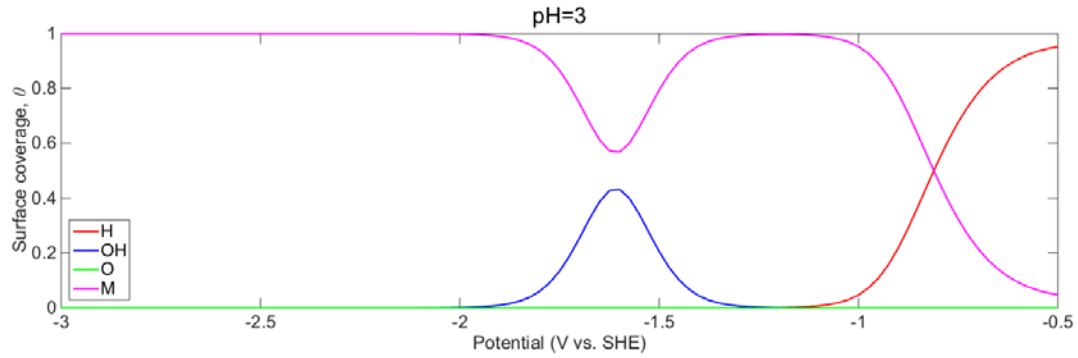
pH=3
Surface coverage, θ
H
OH
O
M
Potential (V vs. SHE)

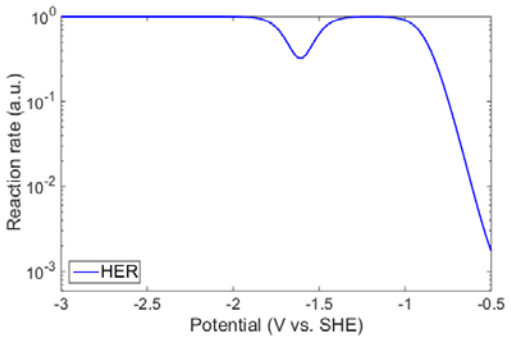
Reaction rate (a.u.)
HER
Potential (V vs. SHE)

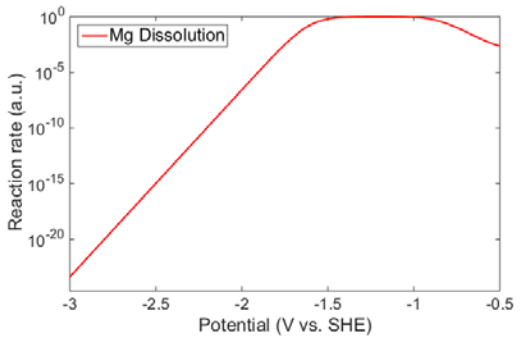
Reaction rate (a.u.)
Mg Dissolution
Potential (V vs. SHE)

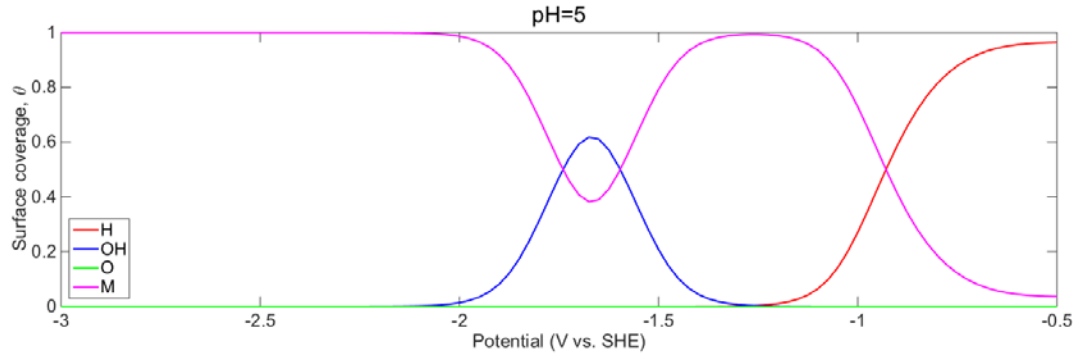
pH=5
Surface coverage, θ
H
OH
O
M
Potential (V vs. SHE)

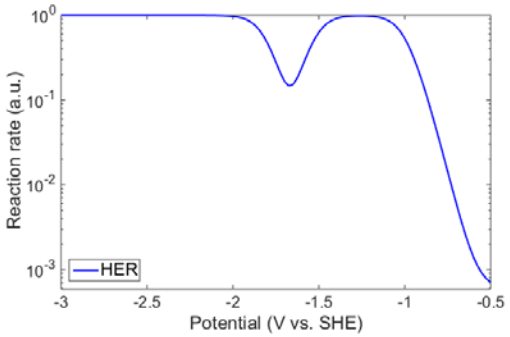
Reaction rate (a.u.)
HER
Potential (V vs. SHE)

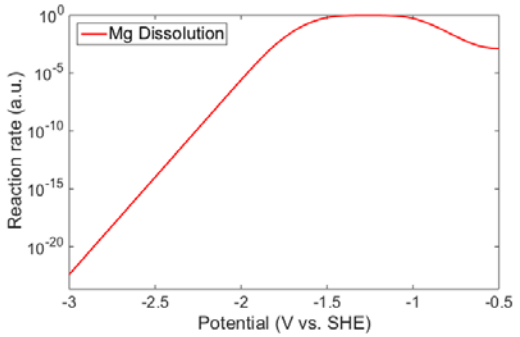
Reaction rate (a.u.)
Mg Dissolution
Potential (V vs. SHE)

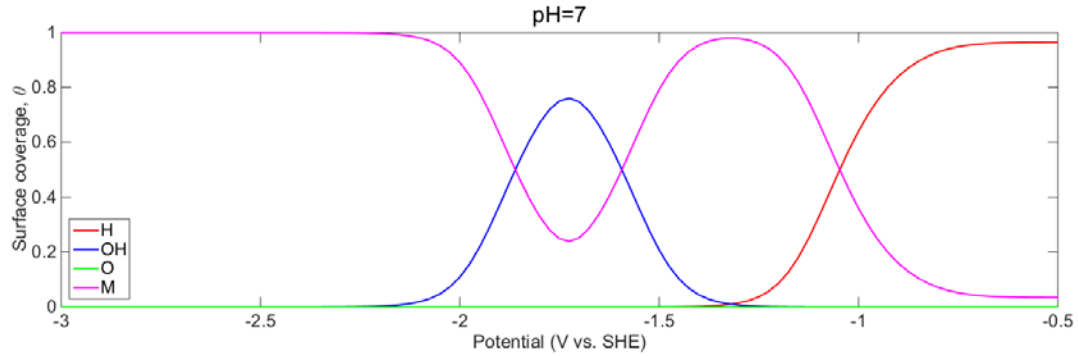
pH=7
Surface coverage, θ
H
OH
O
M
Potential (V vs. SHE)

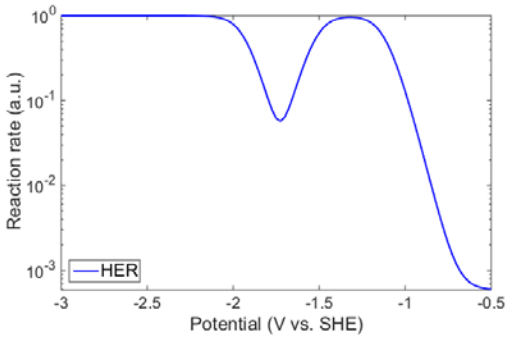
Reaction rate (a.u.)
HER
Potential (V vs. SHE)

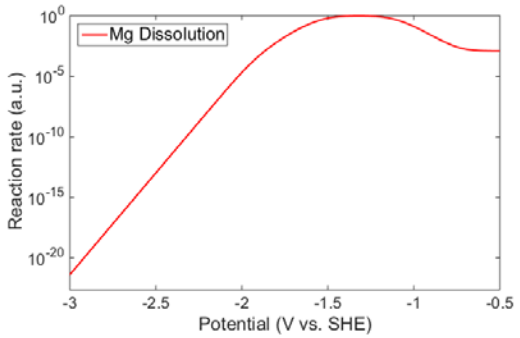
Reaction rate (a.u.)
Mg Dissolution
Potential (V vs. SHE)

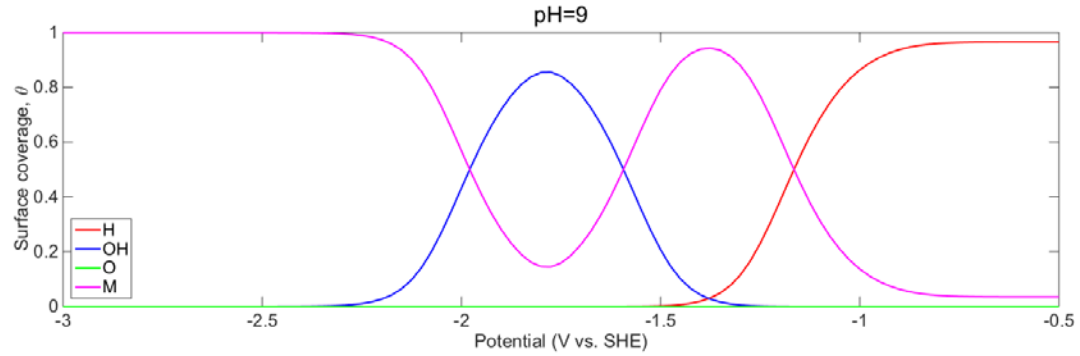
pH=9
Surface coverage, θ
H
OH
O
M
Potential (V vs. SHE)

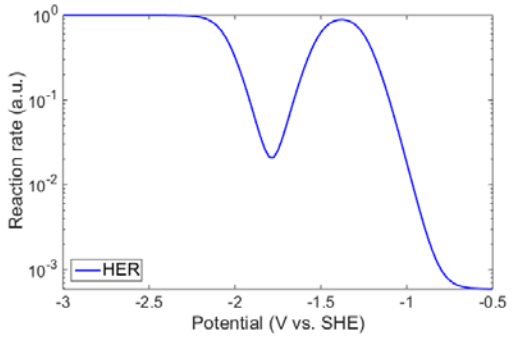
Reaction rate (a.u.)
HER
Potential (V vs. SHE)

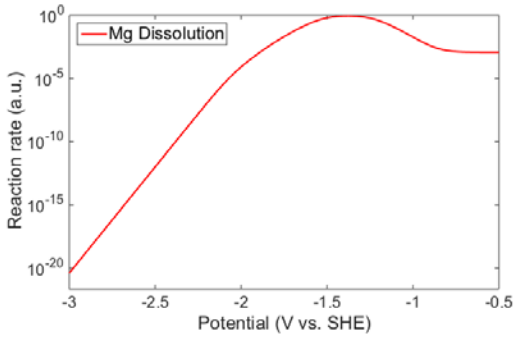
Reaction rate (a.u.)
Mg Dissolution
Potential (V vs. SHE)

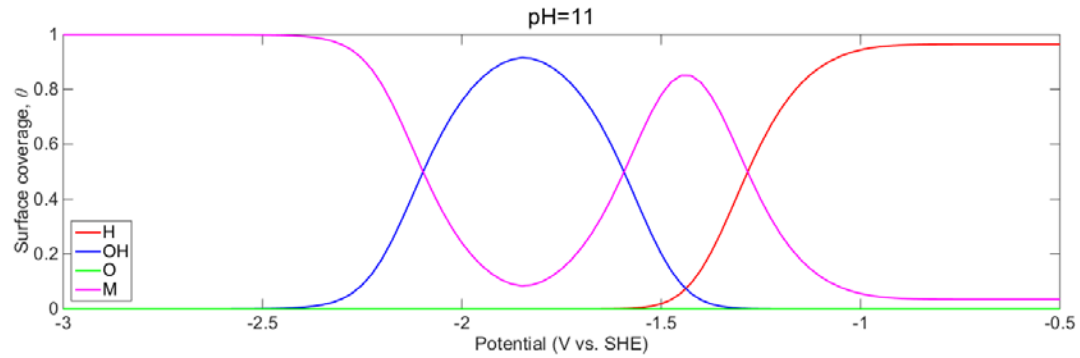
pH=11
Surface coverage, θ
H
OH
O
M
Potential (V vs. SHE)

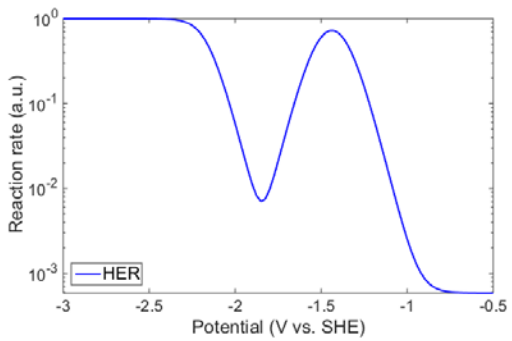
Reaction rate (a.u.)
HER
Potential (V vs. SHE)

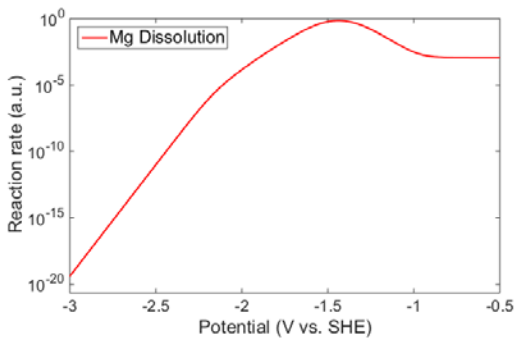
Reaction rate (a.u.)
Mg Dissolution
Potential (V vs. SHE)

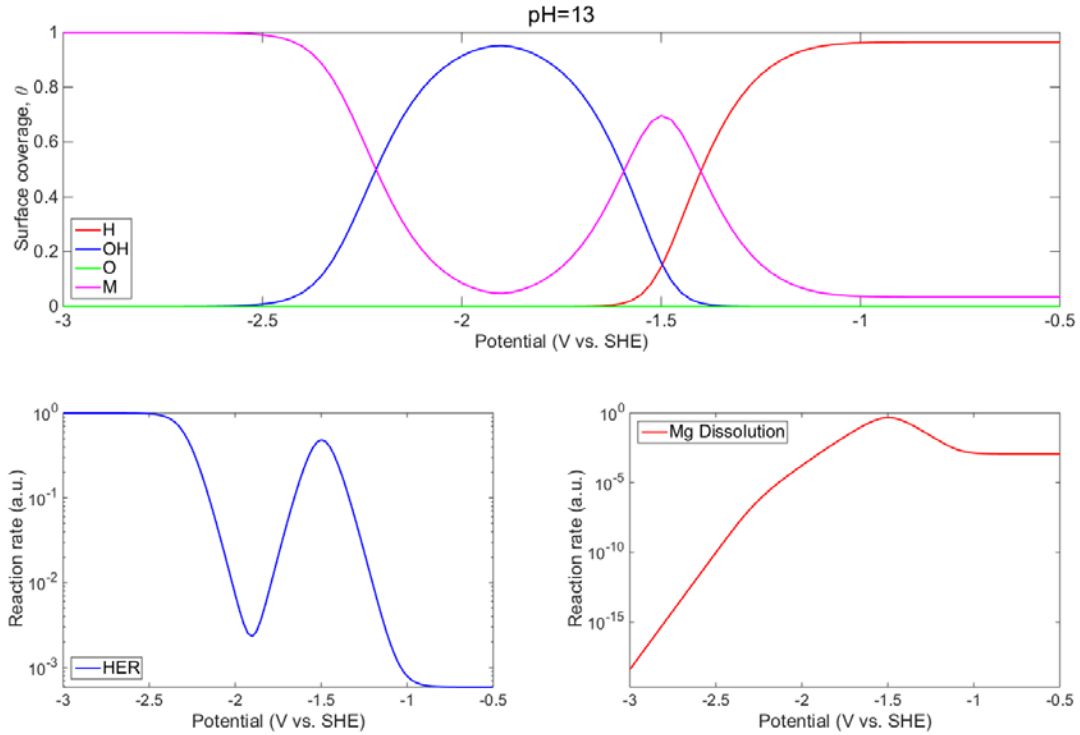

Figure S7. First-principles prediction of fractional surface coverage for free metallic sites, hydroxide-adsorption, oxygen-adsorption and hydrogen-adsorption as the functions of potential and pH

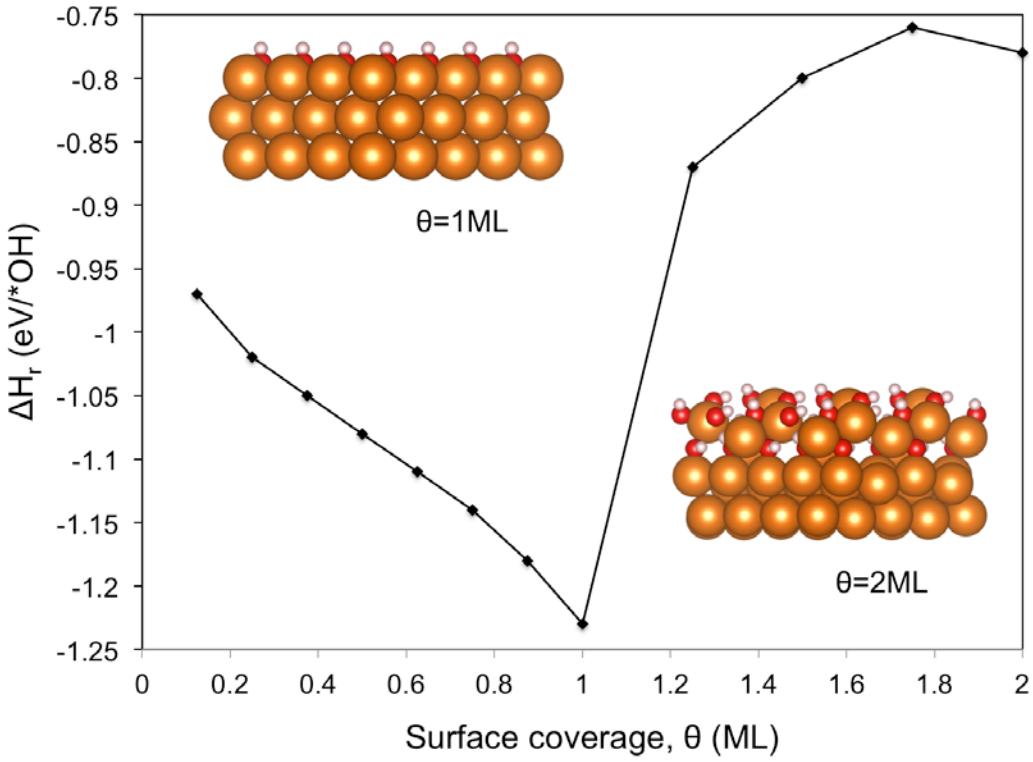

Figure S8. Reaction enthalpy of hydroxylation vs. surface coverage of *OH groups

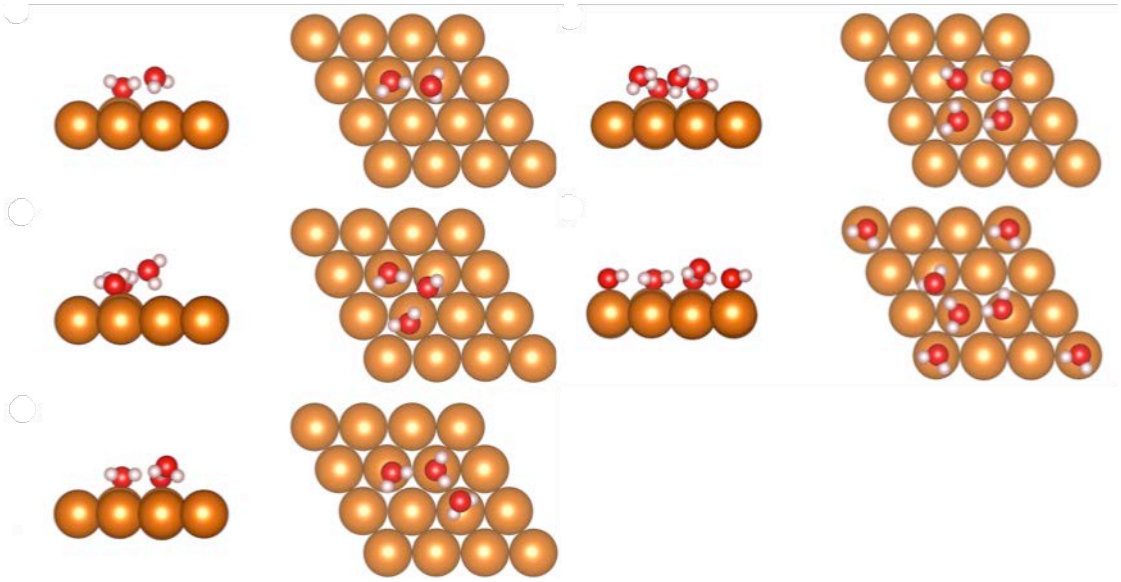

Figure S9. Optimised geometries of Mg/H_2O interface with increasing number of water molecules with (a) dimer, (b) "cyclic" trimer, (c) "open" trimer, (d) "cyclic" tetramer, and (e) "open" tetramer configuration